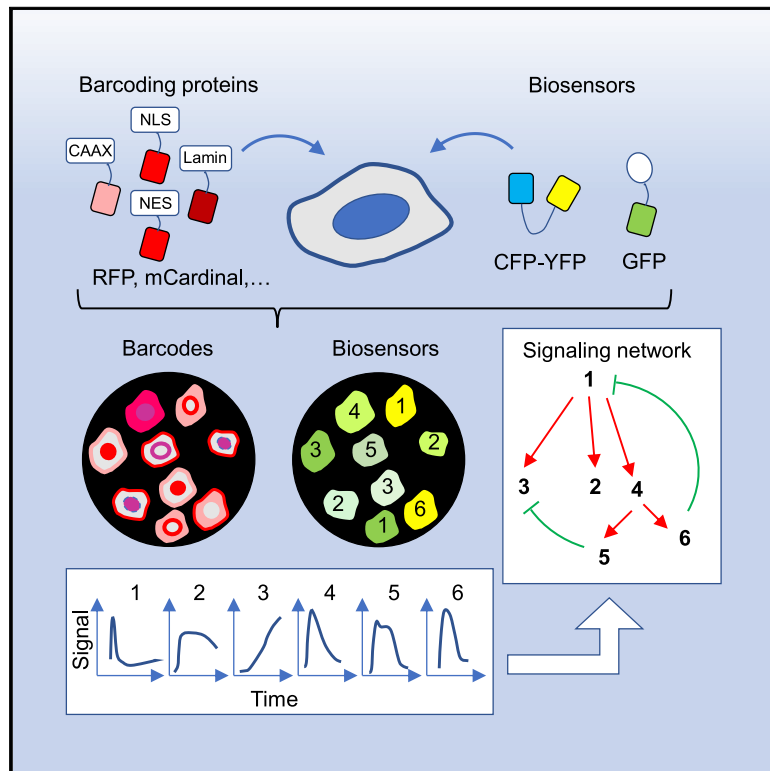


# Deciphering cell signaling networks with massively multiplexed biosensor barcoding

## Graphical abstract



## Authors

Jr-Ming Yang, Wei-Yu Chi, Jessica Liang, Saki Takayanagi, Pablo A. Iglesias, Chuan-Hsiang Huang

## Correspondence

jyang38@jhmi.edu (J.-M.Y.),  
chuang29@jhmi.edu (C.-H.H.)

## In brief

Genetically encoded barcodes that uniquely identify cells expressing a particular fluorescent biosensor enable the simultaneous use of a broader set of biosensors in mixed cell populations and dynamic imaging of many cellular responses in a single experiment to reduce inter-experimental variability when interrogating complex biological interactions, such as the downstream consequences of receptor tyrosine kinase activation, with the help of image-based deep learning models for automated barcode unmixing.

## Highlights

- Large numbers of fluorescent biosensors can be concurrently tracked in barcoded cells
- Biosensor activities are synchronized in mixed populations of barcoded cells
- Deep learning models facilitate image analysis for biosensor barcoding
- Simultaneous biosensor tracking reveals signaling network structures and interactions



## Resource

# Deciphering cell signaling networks with massively multiplexed biosensor barcoding

Jr-Ming Yang,<sup>1,\*</sup> Wei-Yu Chi,<sup>1</sup> Jessica Liang,<sup>2</sup> Saki Takayanagi,<sup>3</sup> Pablo A. Iglesias,<sup>4</sup> and Chuan-Hsiang Huang<sup>1,5,\*</sup><sup>1</sup>Department of Pathology, Johns Hopkins Medical Institutions, Baltimore, MD 21205, USA<sup>2</sup>Department of Biology, Johns Hopkins University, Baltimore, MD 21218, USA<sup>3</sup>XDBio Graduate Program, Johns Hopkins School of Medicine, MD 21205, USA<sup>4</sup>Department of Electrical and Computer Engineering, Whiting School of Engineering, Johns Hopkins University, Baltimore, MD 21218, USA<sup>5</sup>Lead contact\*Correspondence: [jyang38@jhmi.edu](mailto:jyang38@jhmi.edu) (J.-M.Y.), [chuang29@jhmi.edu](mailto:chuang29@jhmi.edu) (C.-H.H.)<https://doi.org/10.1016/j.cell.2021.11.005>

## SUMMARY

Genetically encoded fluorescent biosensors are powerful tools for monitoring biochemical activities in live cells, but their multiplexing capacity is limited by the available spectral space. We overcome this problem by developing a set of barcoding proteins that can generate over 100 barcodes and are spectrally separable from commonly used biosensors. Mixtures of barcoded cells expressing different biosensors are simultaneously imaged and analyzed by deep learning models to achieve massively multiplexed tracking of signaling events. Importantly, different biosensors in cell mixtures show highly coordinated activities, thus facilitating the delineation of their temporal relationship. Simultaneous tracking of multiple biosensors in the receptor tyrosine kinase signaling network reveals distinct mechanisms of effector adaptation, cell autonomous and non-autonomous effects of KRAS mutations, as well as complex interactions in the network. Biosensor barcoding presents a scalable method to expand multiplexing capabilities for deciphering the complexity of signaling networks and their interactions between cells.

## INTRODUCTION

To understand the complex regulatory relationship between signaling, metabolic, and other biochemical activities in cells, it is often necessary to study their dynamics under a multitude of perturbation conditions. Genetically encoded fluorescent biosensors offer a versatile tool to continuously monitor a wide range of biochemical activities in live cells while revealing cell-to-cell variability that is masked in ensemble measurements (Newman et al., 2011; Zhang et al., 2002). A major drawback of fluorescent biosensors is their limited multiplexing capability due to the broad emission spectra of fluorescent proteins (FPs) and limited availability of spectral space (Welch et al., 2011). Efforts have been directed toward expanding the spectral range by developing far-red/infrared fluorophores, replacing two fluorophore biosensors (e.g., those based on fluorescence resonance energy transfer [FRET]) with single-fluorophore designs, and computational multiplexing to reveal the spatiotemporal relationship between biosensors (Chernov et al., 2017; Grant et al., 2008; Machacek et al., 2009; Marston et al., 2020; Mehta et al., 2018; Regot et al., 2014). Despite these improvements, no more than a handful of biosensors can be imaged concurrently. To overcome this limitation, we developed a “biosensor barcoding” method for highly multiplexed tracking of fluorescent biosensors. The key idea is to label cells with barcoding proteins made of different fluorophores targeted to distinct subcellular locations. Combinations of barcoding proteins are then used to generate barcodes that uniquely

identify the cells expressing specific biosensors (Figures 1A–1C). To track multiple activities in parallel, mixed populations of barcoded cells are imaged in a time-lapse microscopy experiment. Activities from cells with the same barcode are pooled together to obtain the temporal profile of the corresponding biosensor (Figures 1D–1F; Video S1). Our method is compatible with any biosensor with emission wavelengths between 450 nm and 550 nm, including the majority of existing FRET or single fluorophore biosensors.

## RESULTS

### Barcoding cells

In theory,  $N$  different barcoding proteins can be combined to create  $2^N$  different barcodes, assuming binary expression (i.e., not expressed or expressed). In reality, the expression of barcoding proteins is a continuum, and low-expressors may be hard to distinguish from nonexpressors, thus precluding the use of all combinations. To ensure robust barcode identification, we only included combinations of two barcoding proteins that were (1) of different colors; and (2) targeted to different subcellular locations. Barcoding proteins also need to be spectrally separable from biosensors. A large number of fluorescent biosensors are based on detecting changes in (1) the intracellular localization or intensity of a single fluorophore, in many cases green FP (GFP), or (2) the FRET efficiency between a donor and an acceptor, most commonly cyan and yellow FPs (CFP and YFP) (Greenwald





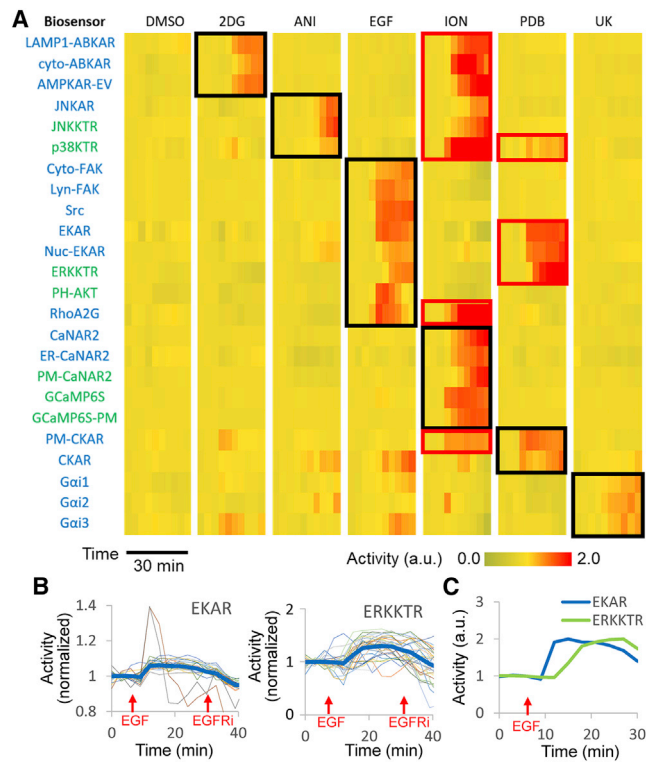


**Figure 2. Multiplexed real-time tracking of biosensor activities in barcoded cells**

(A) Mixed population of barcoded HeLa cells expressing 24 FRET (blue) and non-FRET (green) biosensors (Table S1) were stimulated with the indicated activators (2DG, 10 mM 2-deoxyglucose; ANI, 1  $\mu$ g/mL anisomycin; EGF, 100 ng/mL EGF; ION, 1  $\mu$ M ionomycin; PDB, 200 nM phorbol-12,13-dibutyrate; and UK, 10  $\mu$ M UK14304). For each barcode, the activities were normalized to pre-stimulus levels across cells of the corresponding barcode and adjusted for its dynamic range (Table S2). Black boxes indicate expected responses to known activators. Red boxes indicate additional responses.

(B) Individual cell traces of EKAR and ERKKTR activities normalized to pre-stimulus levels. Thick blue lines represent the average activities.

(C) Comparison of activation kinetics of EKAR and ERKKTR obtained from mixed barcoded cells. Activities are scaled to the peak responses and represent the mean of 46 (EKAR) and 22 (ERKKTR) cells.

See also Table S3.

report ERK activation, but the kinetics of ERKKTR was delayed compared to that of EKAR, consistent with previous observations (Figure 2C) (Pargett et al., 2017; Yang et al., 2018).

To validate the results derived from mixed barcoded cells, we compared the responses to those from a homogeneous population of cells expressing single biosensors. The kinetics of the responses obtained from single-cell populations were in general agreement with those from mixed-cell populations (Table S2). Because all responses initiated between 3–9 min after stimulation, we compared their magnitude at 9 min and found that for the majority (75%) of biosensors, no significant difference was noted between the two groups (Table S2). Analysis of responses 15 min after stimulation produced a similar result (Table S2). For biosensors that showed statistically significant differences, the responses were smaller in the mixed population group in about half of the cases and larger in the remainder. Such variability is expected

among experimental replicates with identical protocols (see the section “Synchrony among biosensors in barcoded cell mixtures” below). To rule out cross-transfection between different barcoded cells (e.g., through carryover of transfection material or exosomes), we mixed cells transfected with single barcoding proteins of different colors and targeting sites. In over 600 cells, no instance of double expression was found, suggesting that cross-transfection is an extremely unlikely event (Figures S1C and S1D).

In addition to the responses to known activators, our analyses revealed unanticipated responses, such as ionomycin-induced activation of AMPK, JNK, p38, RhoA, and PKC, as well as PDBu-induced activation of ERK and p38 (Figure 2A, red boxes). These observations are supported by earlier reports based on a variety of assays in different cell types (Table S3). Taken together, these results demonstrate that (1) the barcodes allow for correct identification of cells expressing different biosensors and are compatible with biosensor imaging without affecting biosensor responses; (2) the technique reveals variations between cells and kinetics of biosensors; and (3) multiplexed biosensor imaging can facilitate comprehensive identification and kinetic characterization of multiple cellular activities.

### Deep learning models for barcode reading

To facilitate the identification of barcoded cells, we developed deep learning models for automated barcode reading. Using deep convolutional neural network models trained on curated images, we classified a testing set of linearly unmixed images of cells expressing pairs of barcoding proteins. The average accuracy was 97%, but varied from 50% to 100% for individual barcodes mostly due to suboptimal unmixing of two red FPs. To overcome this problem, we adopted a new barcoding strategy by pairing BFP with one of the three red FPs targeted to any of the four subcellular locations, generating a total of  $4 \times 4 \times 3 = 48$  different barcodes. We replaced TagRFP with mCherry, which was brighter but harder to unmix with mCardinal in the original barcoding scheme (Figure 3A).

To test the new barcoding scheme for classification by deep learning models, we coexpressed BFP targeted to either the nucleus or plasma membrane along with a red FP targeted to four different subcellular locations in HeLa cells. Spectral images were acquired and unmixed using the reference spectra of mCherry, mCardinal, and iRFP702 to determine the identity of the red FP. The BFP image, once classified, could serve as a reference for red-FP localization. Therefore, we trained three deep learning models to classify (1) BFP images; (2) red FP images combined with nuclear BFP; and (3) red FP images combined with plasma membrane BFP (Figure 3B). We tested the performance of these models on images of barcoded cells and achieved an average accuracy of 99% (range, 92.5%–100%) (Figure 3C). The cause of misidentification included saturating or dim fluorescence signals, the presence of a second cell in the region selected for analysis, and unhealthy or apoptotic cells. The time to analyze one imaging experiment (~300 cells) was less than 10 s using deep learning models (Intel Core i5-7500 CPU @ 3.40 GHz, 3.41 GHz, 32 GB RAM). For comparison, human reading of the same number of barcodes took ~2 h. Together, these results demonstrated that deep learning models can achieve high efficiency and accuracy in barcode reading.



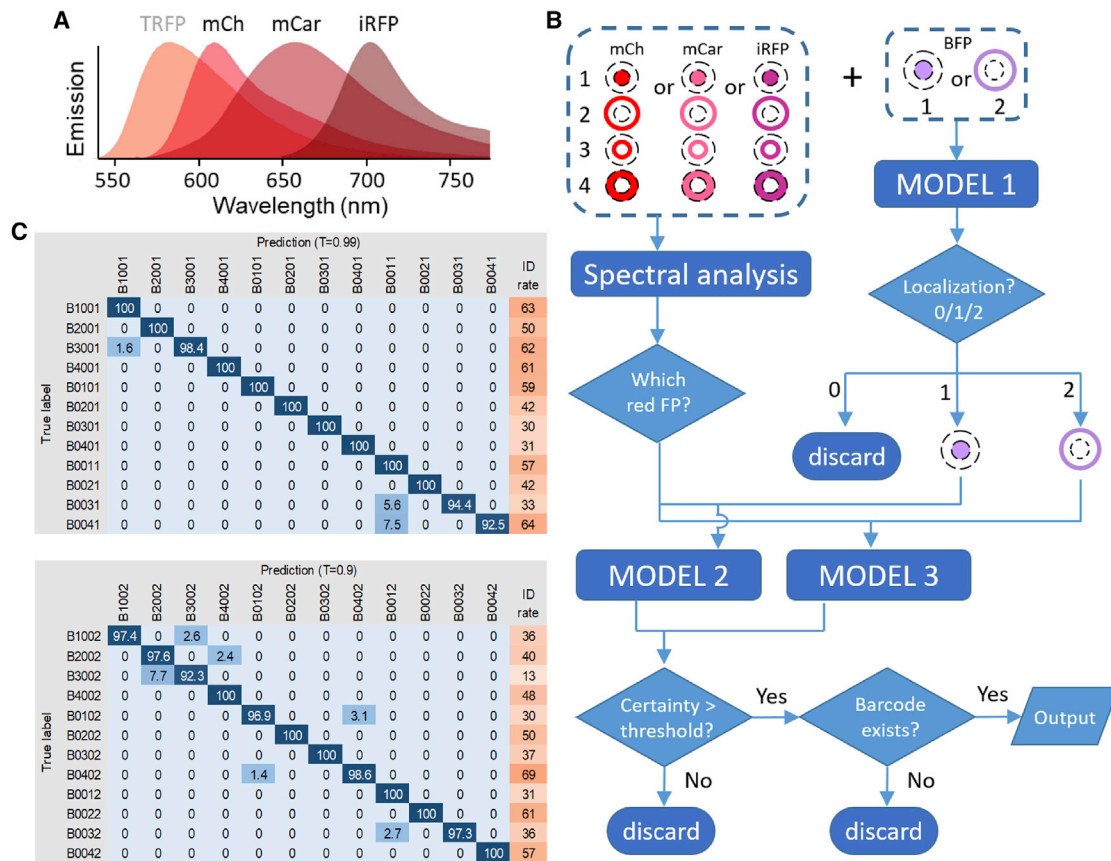


**Figure 3. Barcode reading using deep learning models**

(A) Emission spectra of mCherry (mCh), mCardinal (mCar), and iRFP702 (iRFP) used for barcode reading by deep learning models. TagRFP (TRFP), used in the original barcoding scheme (Figure 1), was replaced by mCherry.

(B) Cells were barcoded by one of the red FPs targeted to four subcellular locations plus BFP targeted to the nucleus or the plasma membrane. The BFP image was classified by model 1. For the red barcoding proteins, spectral profiles were used to determine which of the three unmixed channels corresponded to the correct FP. The unmixed red FP image was then combined with BFP image and classified by model 2 or model 3 depending on whether BFP signal was in the nucleus or membrane. The output was filtered by a certainty threshold and checked for the existence of the barcode.

(C) The confusion matrix and identification rate (%) for all barcodes identified by model 2 (top) and model 3 (bottom) under indicated certainty thresholds. In general, higher certainty thresholds lead to increased accuracy but decreased identification rate. The four numbers in the barcode denote mCherry, mCardinal, iRFP702, and BFP localized to the nucleus (1), plasma membrane (2), nuclear membrane (3), cytosol (4), or non-expressed (0), respectively.

### Expanding the barcoding toolkit

We next sought to extend the success with barcoding HeLa cells to other cell lines, including 293T, MCF7, U87MG, SiHa, U2OS, and A6L, which varied in morphology and transfection efficiency. High transfection efficiency was achieved in 293T, MCF7, and U2OS cells. Most barcodes in these cells were readily identifiable (Figures 4A, 4B, and S2A). Interestingly, in some U2OS cells, plasma membrane-targeted FPs appeared as a broad “haze” that resembled cytosolic signals (e.g., the D2E3 cell in Figure S2A). 3D reconstruction of z-stacks from these cells revealed a “cowboy hat” morphology with extended protrusion of the membrane around the cell periphery (Figure S2B). Although the broad membrane signals might appear cytosolic when examined in isolation, they were still distinct from the cytosolic signal in the same cell (e.g., the D2E4 cell in Figure S2A).

We applied deep learning models to classify images of barcoded 293T, MCF7, and U2OS cells. The models trained on

HeLa images correctly identified 97.8% (range, 94.8%–100%) of barcoded 293T cells (Figure 4C). However, the accuracy was lower for MCF7 (90.1%) and U2OS (81.4%) (Figures 4D and S2C), in part due to the aforementioned broad membrane signals. We therefore trained new models using MCF7 and U2OS images, which achieved accuracy of 99.2% (range, 93.3%–100%) and 98.1% (range, 92.7%–100%) for MCF7 and U2OS cells, respectively (Figures 4D and S2C). These results demonstrate that barcode reading by deep learning models can be generalized to different cell lines.

To overcome the low transfection efficiency in U87MG, SiHa, and A6L cells, we generated lentiviral vectors encoding barcoding proteins using the Gateway recombination system (Figure S3A). Co-transduction of these cells with pairs of lentiviruses led to robust expression of barcoding proteins that were localized to the expected subcellular sites (Figures S3B–S3D). In addition to barcoding a broader range of cell lines, the more

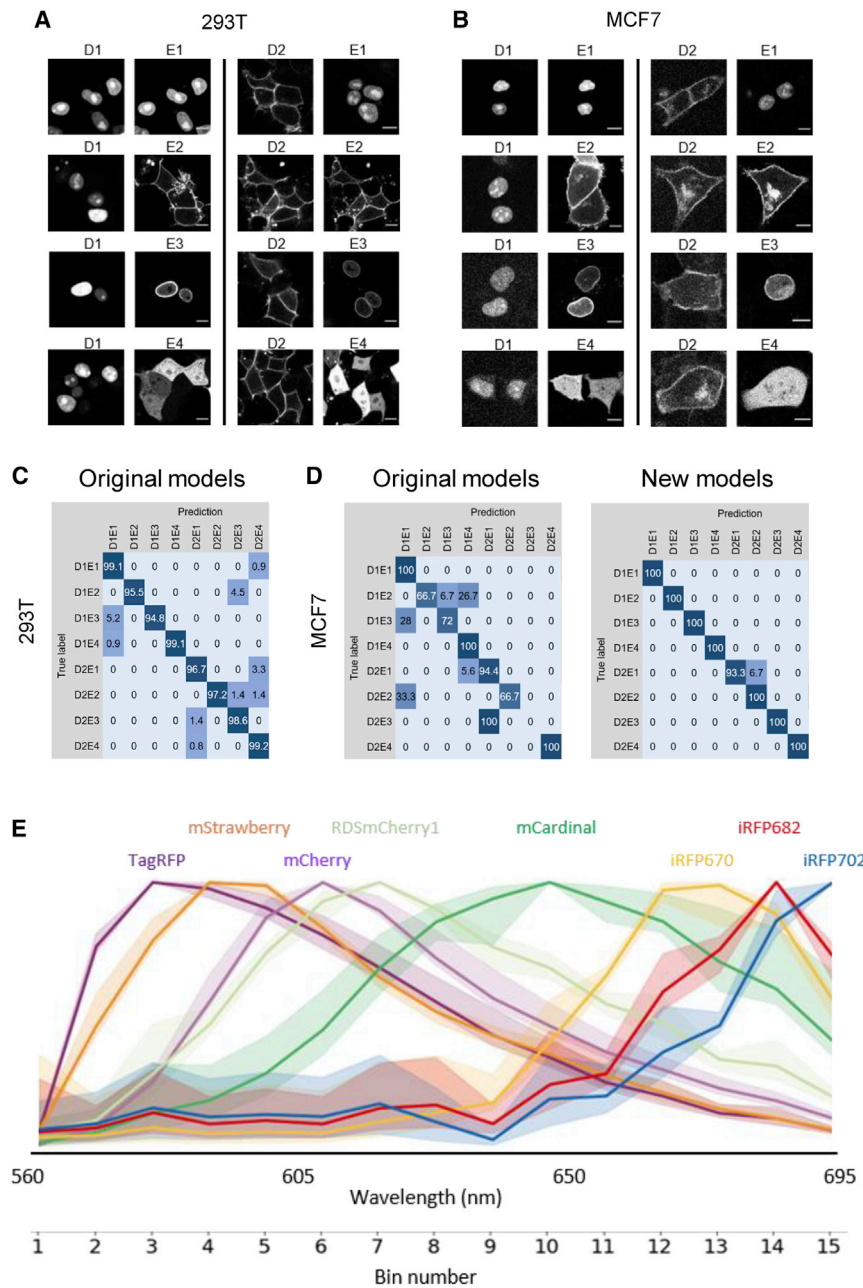


**Figure 4. Expanding the barcoding toolkit**

(A and B) 293T and MCF7 cells transfected with BFP targeted to the nucleus (D1) or plasma membrane (D2) along with mCherry targeted to one of the four subcellular locations (E1, nucleus; E2, plasma membrane; E3, nuclear membrane; and E4, cytosol). Scale bars, 10  $\mu$ m.

(C) Confusion matrix (%) of 293T cells barcoded with nuclear or cytoplasmic BFP plus mCherry targeted to one of the four subcellular locations using the deep learning models trained on HeLa cells.

(D) Confusion matrix (%) of barcoded MCF7 cells using the deep learning models trained on HeLa cells (original models, left) and new models trained on MCF7 cell images (right). See also [Figure S2](#) for U2OS cells.

(E) Emission profiles of red FPs acquired on a Zeiss LSM 780 microscope equipped with a GaAsP detector. For each fluorophore, the curve represents the mean of 100 HeLa cells expressing the nucleus-targeted version of the FP, with the full range of variation shown as shaded area. See also [Table S4](#).

mStrawberry, RDSmCherry1, mPlum, mNeptune, mNeptune2.5, iRFP670, and iRFP682 for testing and acquired their emission profiles by imaging HeLa cells expressing nucleus-targeted versions of these FPs ([Figure 4E](#)). Eight of the FPs (TagRFP, mStrawberry, mCherry, RDSmCherry1, mCardinal, iRFP670, iRFP682, and iRFP702) showed distinct emission peaks in all cells examined ([Figure 4E](#); [Table S4](#)). With four different subcellular localizations, the combination of BFP and one of the eight red FPs can generate a total of  $4 \times 4 \times 8 = 128$  different barcodes. Besides tracking an even greater number of biosensors, the additional fluorophores can compensate for the possible loss of usable subcellular locations in cells with more challenging morphologies.

### Synchrony among biosensors in barcoded cell mixtures

A common problem associated with comparing or combining biosensor mea-

stable expression of lentiviral vectors compared to transient transfections will allow for long-term imaging experiments.

We reasoned that the number of barcodes in the new scheme can be easily scaled up with additional red FPs that are spectrally separable. In this scheme, red FPs were identified by their peak emissions based on the spectral profile acquired using a Zeiss GaAsP detector in 15 bins (of 9 nm each) between 560 and 695 nm. For example, the peaks of mCherry, mCardinal, and iRFP702 fell within bins 6, 10, and 15, respectively ([Figure 4E](#)). Using the spectral information from FPbase ([Lambert, 2019](#)) as a guide, we selected additional red FPs including LSS-mKate2,

surements from multiple experiments is the variability caused by factors such as subtle changes in cell density or temperature. We reasoned that such variability can be minimized by subjecting mixed populations of barcoded cells to a common physicochemical environment, allowing accurate comparison of different biosensors. To test this idea, we examined the results of ten experimental replicates in which barcoded cells expressing PH-AKT, EKAR, nuc-EKAR, Src, and Lyn-FAK biosensors were stimulated with EGF. Despite identical settings, variations in the timing and amplitude of the responses were noted ([Figure 5A](#)). We fitted individual traces to a biphasic exponential

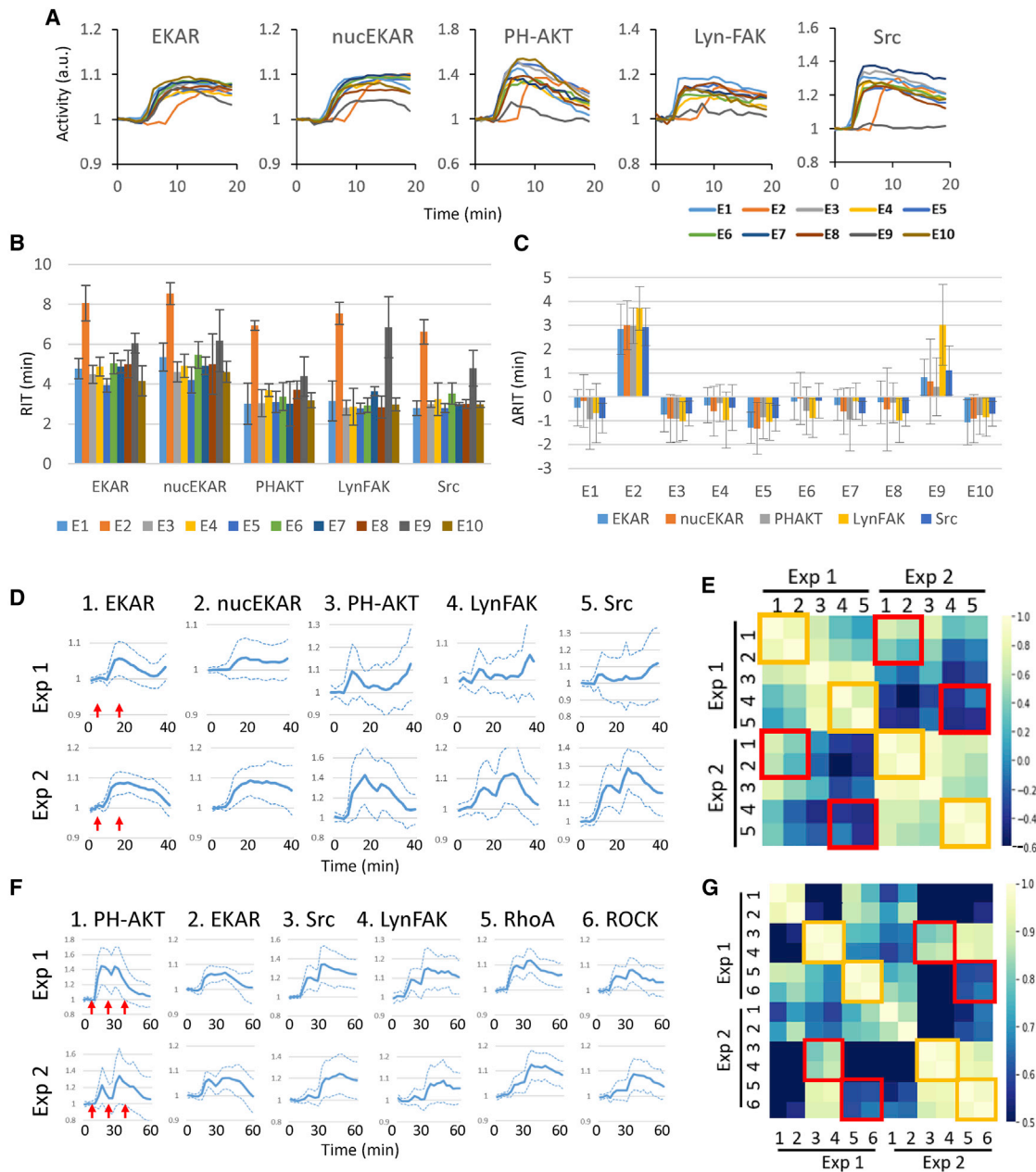


**Figure 5. Synchrony between biosensors in mixed barcoded cells**

(A) Responses of biosensors obtained from mixed barcoded cells stimulated with 10 ng/mL EGF, added 2 min after imaging started. Traces of mean responses are shown in different colors for ten experimental repeats (E1–E10).

(B) Response initiation time (RIT) for each biosensor based on the traces in (A) (see STAR Methods and Figure S4). Error bars, 95% confidence interval.

(C)  $\Delta$ RIT, defined as individual RIT minus the average RIT across the ten experiments for each biosensor. Error bars, 95% confidence interval.

(D) Biosensor responses from mixed barcoded cells stimulated with 0.5 and 10 ng/mL EGF at 4 and 18 min (red arrows), respectively. Traces of mean  $\pm$  SD from two experiments are shown.

(E) Cross-correlation between the responses of different biosensors between the same and different experiments from (D).

(F) Biosensor responses from mixed barcoded cells stimulated with 1, 10, and 100 ng/mL EGF at 6, 21, and 36 min (red arrows), respectively. Traces of mean  $\pm$  SD from two experiments are shown.

(G) Cross-correlation between the responses of different biosensors between the same and different experiments from (F). In (E) and (G), boxes indicate pairs of biosensors detecting the same proteins (ERK) or one protein and its immediate effector (Src/FAK or RhoA/ROCK) from the same (yellow boxes) or different (red boxes) experiments.

See also Data S1.



model to obtain the response initiation time (RIT) of the responses (Figures 5B and S4). Comparison of the RITs of individual experiments and those averaged across ten experiments indicated that different biosensors were synchronized in the same experiment despite significant variabilities between experiments (Figure 5C).

We next examined the responses to more complex stimulation schemes by treating barcoded cells expressing EKAR, nucEKAR, PH-AKT, Lyn-FAK, and the Src biosensor sequentially with 0.5 and 10 ng/mL EGF. In two experimental repeats, the response to the second stimulus was delayed in one but immediate in the other (Figure 5D). Cross-correlation analyses showed higher similarities within the same experiment than between experiments (Figure 5E). Notably, in the same experiment, highest correlation occurred between the two ERK biosensors, EKAR and nucEKAR, and between biosensors for FAK and Src, which are known to activate each other through direct interactions (Frame et al., 2010) (Figure 5E, yellow boxes). The correlation between these two pairs of biosensors was much lower across different experiments (Figure 5E, red boxes). In a second set of experiments in which cells were stimulated with 1, 10, and 100 ng/mL EGF (Figure 5F), a high correlation was noted between biosensors for Src and FAK and between those for RhoA (Fritz et al., 2013) and ROCK (Li et al., 2017) within the same experiment (Figure 5G, yellow boxes) but not between two experimental repeats (Figure 5G, red boxes). Note that ROCK is a downstream effector of RhoA through direct binding (Amano et al., 2010). Therefore, the strong correlation between biosensor pairs is consistent with known interactions between signaling proteins. Together, the above results suggest a high degree of synchronization among the activities of different biosensors in the same experiment and significant variations of the same biosensor across different experiments.

### Interrogating the kinetics of signaling networks

We next investigated the responses of the receptor tyrosine kinase (RTK) signaling network to EGF and inhibitors. After testing 28 biosensors for their responsiveness to EGF (Table S1), we selected 10 responders that detected the activity of the RTK/EGF receptor (EGFR) as well as its multiple downstream effectors, including PI3K, Syk, ERK, calcium, RhoA, Src, S6K, FAK, and ROCK (Figure 6A). We used biosensor barcoding to simultaneously record their responses to 100 ng/mL EGF, and the results from two representative experiments are shown in Figure 6B. PicchuEV, an RTK biosensor (Komatsu et al., 2011), showed a gradual increase in activity before reaching a plateau at ~12 min after stimulation. Interestingly, the downstream biosensors displayed varying degrees of adaptation after reaching the peak level. Importantly, the adaptation of all downstream effectors except S6K started while PicchuEV activity was still increasing. To rule out the possibility that RTK inactivation was not detected by PicchuEV in real time, we treated EGF-stimulated cells with the EGFR inhibitor gefitinib and found immediate decrease in PicchuEV activity (Figure S5A). Therefore, the plateauing of the PicchuEV signal indicated continued RTK activation, and downstream adaptation was not caused by RTK inactivation.

We investigated the responses to different concentrations of EGF. As expected, higher EGF generally induced greater re-

sponses (Figure 6C). However, the temporal profile of the responses displayed unique features that fell into three classes: (1) stimulus-dependent plateau; (2) stimulus-dependent adaptation; and (3) all-or-none (Figure 6D). Class 1 included only one biosensor, PicchuEV, which reached a plateau level determined by the stimulus level. Class 2 included Syk, Src, FAK, RhoA2G, EV-ROCK, and S6K, which reached a stimulus-dependent peak level followed by adaptation at various rates. (Note that the seemingly non-adapting response of Syk at the highest EGF dose was caused by a delayed second peak induced by continued receptor activation in some experiments, e.g., Exp 1 in Figure 6B.) Class 3 included GCaMP6S, PH-AKT, and EKAR, which responded with a stimulus-independent peak to EGF above a threshold level. To determine the level of cooperativity for different responses, we fit the peak response versus EGF concentration to a Hill equation (Figure 6E). Whereas class 1 and 2 responses had Hill coefficients close to 1 and thus were noncooperative, class 3 responses showed strong cooperativity with high Hill coefficients, consistent with previous studies on PI3K and ERK signaling (Huang and Ferrell, 1996; Shindo et al., 2016; Zhan et al., 2020).

To check whether partial responses may result from averaging across all-or-none responders, we examined the responses of individual cells to escalating doses of EGF. For class 1 and 2 biosensors, the responses triggered by 1 ng/mL EGF were smaller than those triggered by 10 ng/mL EGF (Figure S5B; note that 100 ng/mL EGF failed to trigger a third response in most cells likely due to previous responses). In contrast, the responses of class 3 biosensors were independent of EGF doses. Therefore, the dose response features of different classes arose at the level of individual cells.

We noticed that EGF triggered transient spreading of cells driven by actin polymerization, as detected by recruitment of LifeAct (Riedl et al., 2008) to the protrusions (not shown). To test the possible involvement of actin in adaptation, we pre-treated cells with jasplakinolide or latrunculin B, which stabilizes or inhibits actin polymerization, respectively. Neither jasplakinolide nor latrunculin B blocked the adaptation of class 2 and class 3 responses (Figures S5C and S5D), suggesting that actin dynamics are not required for adaptation. Interestingly, the responses of RhoA2G, EV-ROCK, and GCaMP6S were greatly diminished, suggesting a possible role of actin in RhoA, ROCK, and calcium activation.

We reasoned that the kinetic and dose response features of different biosensors reflect the topology of regulatory interactions. Specifically, in class 1 responses, the dose-dependent plateaus can be described by a simple binding model (Figure S6A). In class 2 responses, adaptation to continued stimulation can result from either negative feedback (NFB) or incoherent feedforward loop (IFFL) mechanisms (Hoeller et al., 2014; Ma et al., 2009). In both NFB and IFFL models, larger stimuli trigger responses with greater amplitude, but in IFFL, the rate of decay is faster in multiple simulation settings, leading to shorter overall responses (Iglesias and Shi, 2014; Tu and Rappel, 2018). Because class 2 responses did not show a stimulus-dependent change in the decay rate of adaptation (Figure 6D), we chose the NFB model in our simulation (Figure S6B), although an IFFL mechanism cannot be completely ruled out. Finally, for class 3 responses, the all-or-none features are characteristic of excitable networks, which generally involve



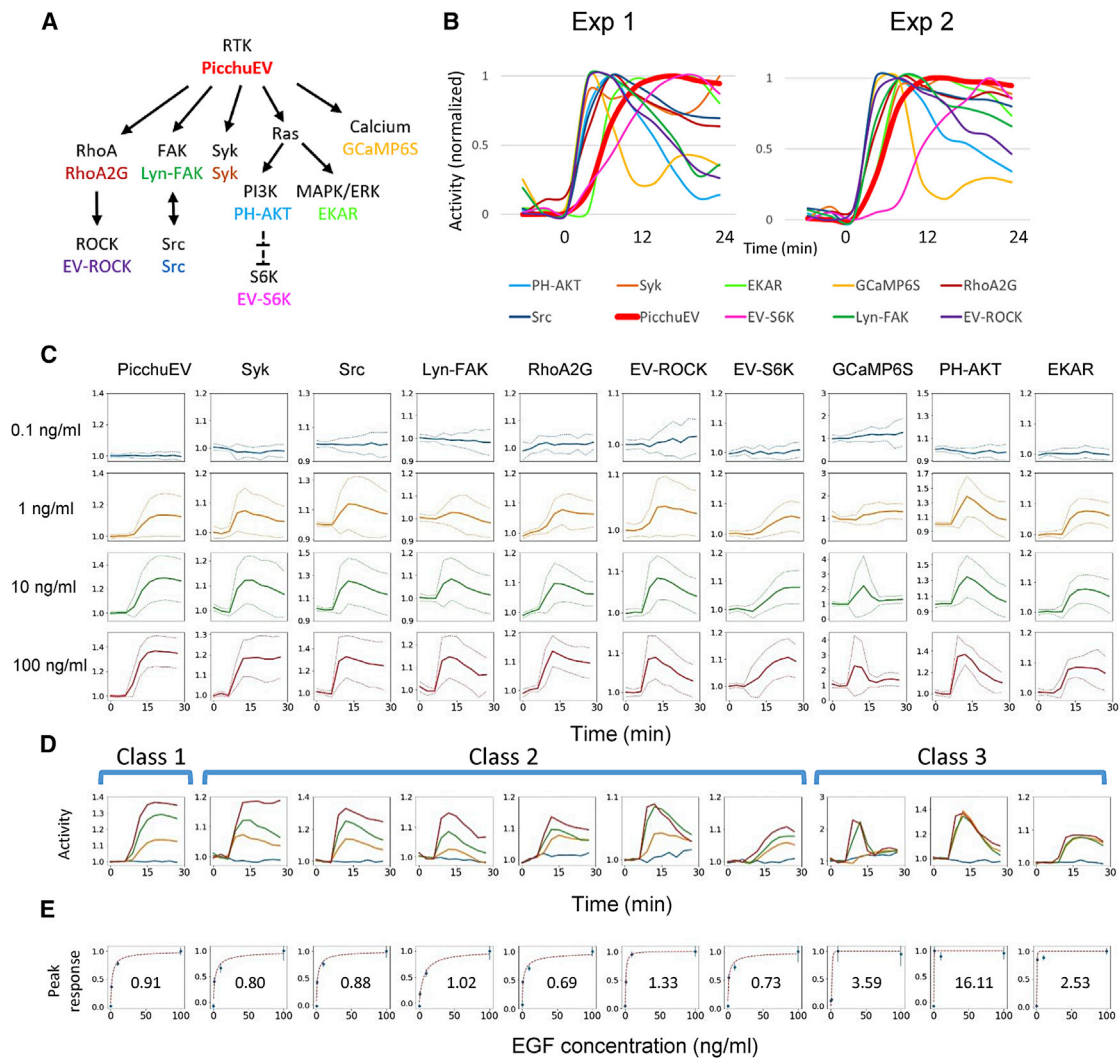


**Figure 6. Responses to RTK stimulation**

(A) 10 biosensors (in color) and their targets mapped to the RTK signaling network.

(B) Responses scaled to the peak levels of the 10 biosensors to 100 ng/mL EGF stimulation at 0 min in mixed barcoded cells from two independent experiments.

(C) Responses of biosensors in barcoded cells to four concentrations of EGF, applied at 6 min. The vertical axes represent biosensor activity (mean  $\pm$  SD of cells from 5 independent experiments) normalized to the prestimulus levels

(D) Activities in (C) plotted on the same graph. The biosensors were grouped into three classes based on their kinetic and dose-response features (see text).

(E) Peak responses (mean  $\pm$  SEM) at different EGF doses, normalized to the peak levels induced by 100 ng/mL EGF, fit to a Hill equation (red dashed line, with the Hill coefficient shown).

See also [Figures S5](#) and [S6](#).

a positive feedback, or autocatalytic loop, that drives a full response once a threshold is crossed, as well as a delayed negative feedback loop that shuts off the response (Xiong et al., 2010) (Figure S6C). We carried out computational simulations of mathematical models representing different network topologies. With appropriate selection of model parameters, we were able to recapitulate the experimentally observed dose response kinetics.

### Delineating cell autonomous and non-autonomous interactions of signaling networks

The ability to barcode different cell populations in a mixture allows for the discrimination between cell autonomous and non-

autonomous interactions. As a demonstration, we investigated the effects of mutant KRAS, one of the most frequent drivers of cancer. Taking advantage of the membrane localization of KRAS by farnesylation, we used BFP-fused KRAS as a barcoding protein. Expression of BFP-fused wild-type KRAS had no effect on the activity of the RAS effector ERK, whereas expression of BFP-fused oncogenic (G12V) and dominant-negative (S17N) mutants of KRAS led to persistently elevated and suppressed ERK activities, respectively, suggesting that BFP fusion did not affect the function of KRAS and its mutants (Figure S7A).

We used biosensor barcoding to examine the responses of HeLa cells expressing KRAS(G12V). Compared to the

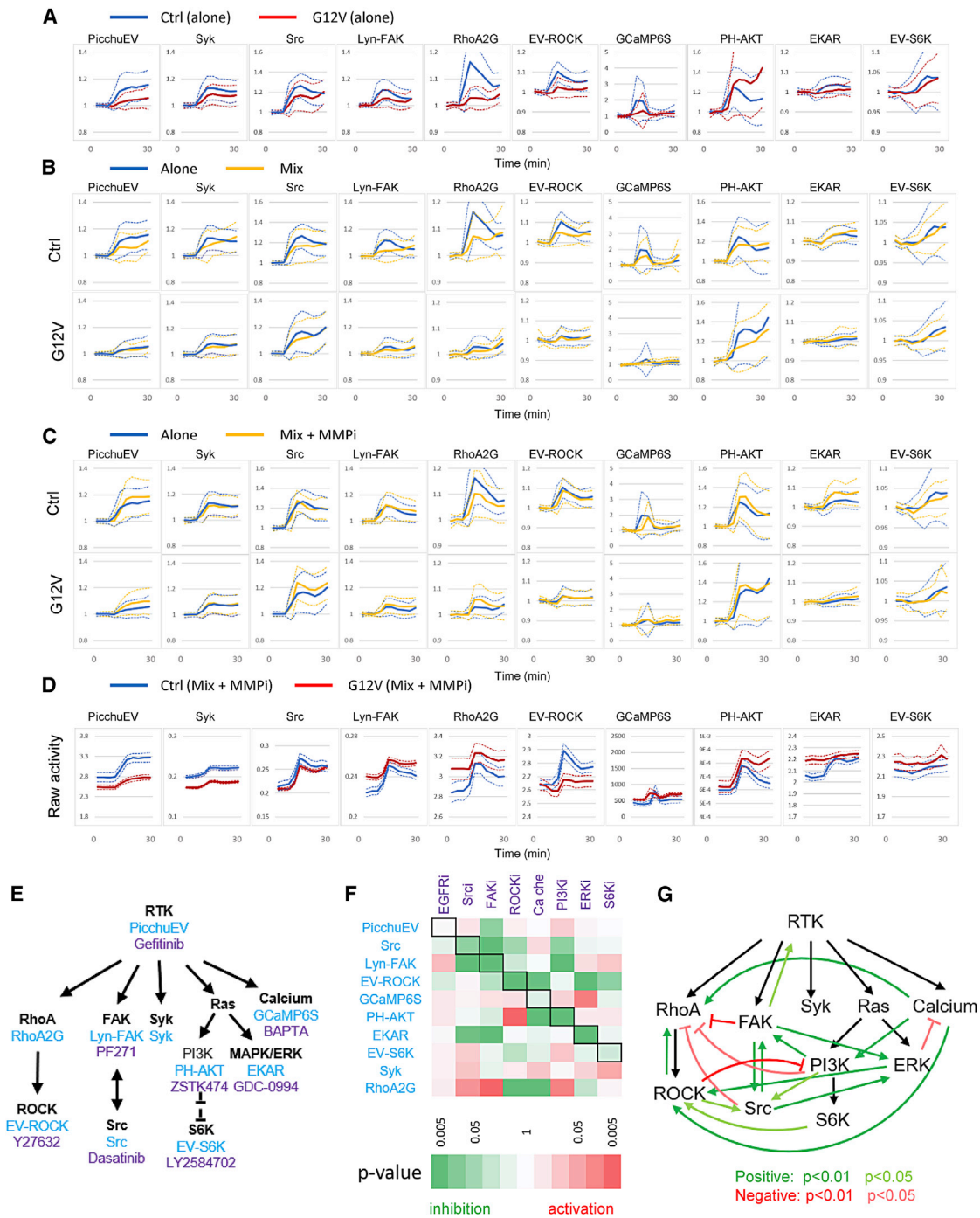


**Figure 7. Interactions between pathways and cells**

(A) Normalized responses (mean  $\pm$  SD) of control cells alone and KRAS(G12V) cells alone to 100 ng/mL EGF stimulation added at 6 min.

(B) Normalized responses (mean  $\pm$  SD) of control and KRAS(G12V) cells in a 1:1 mix to 100 ng/mL EGF (yellow). The responses of control and KRAS(G12V) cells when they were separately stimulated with 100 ng/mL EGF were plotted for comparison (blue). See also Figure S7.

(C) Normalized responses (mean  $\pm$  SD) of control and KRAS(G12V) cells in a 1:1 mix to 100 ng/mL EGF with pretreatment of 10  $\mu$ M TAPI-1 (MMPi, matrix metalloproteinase inhibitor) for 1 h prior to the experiments (yellow). The responses of control and KRAS(G12V) cells when they were separately stimulated with 100 ng/mL EGF were plotted for comparison (blue).

(D) Comparison of raw activities (mean  $\pm$  SEM) of control and KRAS(G12V) cells in a 1:1 mix pretreated with 10  $\mu$ M TAPI-1 (MMPi) and stimulated with 100 ng/mL EGF. The raw activities represent mean  $\pm$  SEM of YFP/CFP (for PicchuEV, RhoA-2G, EV-ROCK, EKAR, and EV-S6K), CFP/YFP (Syk, Src, and Lyn-FAK), cytosolic fluorescence (GCaMP6S), or 1/cytosolic fluorescence (PH-AKT).

(legend continued on next page)

stereotypical EGF responses of control cells, KRAS(G12V)-expressing cells had smaller responses that were often followed by a second peak (Figure 7A) and showed significant variability between experiments (Figure S7B). Next, we mixed barcoded control and KRAS(G12V) cells before stimulation with EGF. Interestingly, the control cells in the mixture displayed smaller, biphasic responses (Figure 7B, top) with increased experimental variability (Figure S7C), suggesting cell non-autonomous effects mediated by KRAS(G12V) cells. The responses of KRAS(G12V) cells were similar regardless of the presence or absence of control cells (Figure 7B, bottom). We surmised that KRAS(G12V) may exert their effect through metalloproteinases of the MMP or ADAM families, which have been shown to release EGFR ligands that mediate the propagation of ERK activation across cell populations (Aoki et al., 2013). To test this hypothesis, we pretreated the control-KRAS(G12V) mixture with the MMP/ADAM inhibitor (MMPi) TAPI-1 before stimulation. Indeed, the effects of KRAS(G12V) cells on the control cells were largely eliminated (Figure 7C). Because cells in the same mix are synchronized (Figure 5), we reasoned that the “raw activity” of mixed control and KRAS(G12V) cells can be directly compared using non-normalized FP fluorescence (Figure 7D). As expected, EKAR showed a high basal activity that was not further activated by EGF in KRAS(G12V) cells, apparently due to direct activation by the constitutively active KRAS mutant. Interestingly, the activities were altered in several other biosensors in KRAS(G12V) cells. We verified the effects of KRAS(G12V) on FAK and ERK by immunoblotting (Figure S7D). Together, these results reveal the distinct effects of KRAS(G12V) on different nodes in the RTK signaling network through both cell-intrinsic and paracrine mechanisms.

We interrogated the interactions within the RTK signaling network by tracking the biosensor responses to a panel of inhibitors targeting different nodes (Figure 7E; Table S5). To quantify the effects of each inhibitor, we integrated the changes in biosensor activity over time, and compared the effects to those of the vehicle control. In addition to the expected targets, several inhibitors altered the activities of other nodes in the network (Figure 7F). Inhibitory and activating effects of the inhibitors on each node suggest positive and negative interactions, respectively (Figure 7G). It should be noted that some of these interactions may be indirect or may result from off-target effects of the inhibitors, and are likely cell-type specific. Nevertheless, the results highlight the complex regulatory relationships between nodes in the RTK signaling network and represent a powerful strategy to discover unknown interactions within signaling networks in cells of interest. Together, our results demonstrated the power of biosensor barcoding in delineating both cell autonomous and non-autonomous interactions within signaling networks.

## DISCUSSION

There has been an increasing need to track multiple biosensors simultaneously for various applications. In one study, three different cell populations expressing biosensors targeted to distinct subcellular locations were co-cultured for simultaneous imaging (Fujita et al., 2014). In this strategy, the multiplicity is limited to the number of sites that can be robustly distinguished in microscopic images. To our knowledge, the only generalizable approach for multiplexing biosensor imaging is the recently reported “signaling reporter islands” method, in which different biosensors are clustered at different spots in cells to allow for spatial separation of their signals (Linghu et al., 2020). However, the method is technically demanding, requiring laborious post-imaging sample processing and analysis to identify the biosensor in each cluster, and is incompatible with translocation based biosensors. The need to engineer and test individual scaffolds used for clustering also makes this method not easily scalable. More generally, one concern about expressing multiple biosensors in the same cells is the possible interaction or interference between the biosensors. Our biosensor barcoding method overcomes these problems by providing a simple way to simultaneously track large numbers of existing fluorescent biosensors, whether they are based on FRET, intensity, or translocation, as long as their emission falls within the CFP to YFP (450 nm to 550 nm) spectral range.

High-throughput imaging can also be used to track large numbers of biosensors in parallel (Chapnick et al., 2019; Kuchenov et al., 2016). However, we demonstrated substantial variation in biosensor activities obtained from physically segregated cell populations. Importantly, we found that mixing cells expressing different biosensors synchronized their responses to perturbations, as demonstrated by the coordinated activities within the same imaging experiment but not between experimental replicates. The cause of variation between experiments is unclear in most cases but likely involves a combination of subtle differences in physical, chemical, and biological factors such as temperature, cell density, nutrient levels, or metabolic states of cells. In addition to the synchronization of biosensor activities, the ability of our method to identify distinct cell populations in a mixture is hard to achieve using other approaches, and will find broad applications in studying cell-cell interactions.

Using biosensor barcoding, we found distinct kinetic properties of multiple downstream pathways in the RTK signaling network. In particular, the all-or-none responses of PH-AKT and EKAR to increasing EGF stimuli add to a growing list of evidence for excitability of the Ras-PI3K-ERK signaling network, including wave-like propagation of activities, refractoriness to repeated stimuli, and characteristic spatiotemporal responses to disruptions in wave patterns (De Simone et al., 2021; Fukushima et al., 2019; van Haastert et al., 2017; Hiratsuka et al., 2015;

(E) Biosensors (blue) and inhibitors (purple) targeting the RTK signaling network.

(F) Inhibition matrix showing the effect of inhibitors on biosensor activities. The effect of an inhibitor on a biosensor was calculated by integrating the activity for all time points after the inhibitor was added minus that of DMSO control. Black boxes denote biosensors corresponding to the targets of inhibitors. Positive and negative effects are shown in red and green, respectively, and the statistical significance is represented by the color scale. See also Table S5.

(G) Feedback loops inferred from the inhibition matrix. Positive (green) or negative (red) interactions were assigned when an inhibitor caused an inhibition or activation, respectively, of another node in the network.

Yang et al., 2016, 2018; Zhan et al., 2020). Calcium waves have also been reported to display features of excitable systems in various tissues (Gelens et al., 2014). Interestingly, we found that calcium responses were also all-or-none but with a higher threshold compared to PI3K and ERK responses, suggesting that calcium signaling belongs to a different excitable network. Moreover, although extensive crosstalk exists between Ras-PI3K-ERK signaling and other downstream effectors of RTKs, the responses of FAK, Src, Syk, and Rho GTPase were not excitable but showed dose-dependent adaptation that likely involves negative feedback mechanisms. The molecular basis of the features displayed by different classes of effectors will be key to understanding the structure and function of the RTK signaling network, which is the target of many clinically approved therapeutics.

Given the ever-growing list of fluorescent biosensors, with a recent review listing over a thousand designs for ~170 cellular targets including enzymes, voltage, ions, and metabolites (Greenwald et al., 2018), we envision our method to find a wide range of applications, such as reconstructing complex molecular networks, delineating the signaling interaction between different cell types, and identifying molecular pathways targeted by pharmacological agents, some examples of which are shown in Figure 7. In addition, biosensor barcoding can facilitate the development of new biosensors through side-by-side comparison of the sensitivity and dynamic range of multiple biosensor designs. Newly developed biosensors will then further expand the biosensor barcoding technique. Although we only demonstrated the use of barcoding for CFP-YFP FRET- and GFP-based biosensors, our technique can be readily adapted to other types of fluorescent or bioluminescent biosensors with similar emission spectra.

### Limitations of study

The rich kinetic data from simultaneous recording of signaling activities will inform the formulation of more comprehensive network models, which hold promise for predicting the responses to genetic or pharmacological perturbations with greater accuracy. In this study, we used simultaneous tracking of biosensors to construct mathematical models that captured salient features of the RTK signaling responses to different concentrations of EGF. For each downstream effector, a model of the receptor-effector pair was created and fitted using synchronized data from both, but different effectors were modeled separately. Similarly, an interaction map was built from the integrated response of biosensors to inhibitors, but a quantitative model describing the temporal changes of all measured responses has yet to be achieved. To take full advantage of the synchronized recording, it is theoretically possible to encompass all effectors in a comprehensive model that is constrained by the kinetic data. One hurdle is that as the number of interactions increases, the complexity of the model rises greatly and finding unique parameter values and model structures becomes difficult. Moreover, the models assume a linear correspondence between the biosensor signal and its target activity, which may not have been fully validated across the measured range of some biosensors. Nevertheless, we envision that the vast amount of data obtained from parallel recording of large numbers of

biosensors upon various perturbations will motivate further development of computational tools for quantitative modeling of complex biological networks.

### STAR★METHODS

Detailed methods are provided in the online version of this paper and include the following:

- KEY RESOURCES TABLE
- RESOURCE AVAILABILITY
  - Lead contact
  - Materials availability
  - Data and code availability
- EXPERIMENTAL MODEL AND SUBJECT DETAILS
- METHOD DETAILS
  - Plasmids
  - Chemical reagents
  - Lentivirus production and transduction
  - Microscopy
  - Image analysis
  - Barcode image classification by deep learning models
  - Fitting responses to kinetic models
  - Simulation of RTK network responses to EGF stimulation
  - Hill equation fitting
- QUANTIFICATION AND STATISTICAL ANALYSIS

### SUPPLEMENTAL INFORMATION

Supplemental information can be found online at <https://doi.org/10.1016/j.cell.2021.11.005>.

### ACKNOWLEDGMENTS

We would like to thank Hoku West-Foyle and Takanari Inoue for helpful discussions, as well as Michiyuki Matsuda for plasmids of PicchuEV, Prin-BRAF, Prin-CRAF, EV-RSK, EV-ROCK, and EV-S6K. Zeiss LSM 780 and 880 confocal microscopes were purchased with NIH grants S10OD016374 and S10OD023548, respectively. This work was supported by NIH (K22CA212060 and R01GM136711 to C.-H.H.), Cervical Cancer SPORE P50CA098252 (Career Development Award to J.-M.Y., Pilot Project Award to C.-H.H.), the W.W. Smith Charitable Trust (C1901 to C.-H.H.), and the Sol Goldman Pancreatic Cancer Research Center (to C.-H.H.).

### AUTHOR CONTRIBUTIONS

J.-M.Y. and C.-H.H. conceived the project and designed the experiments. J.-M.Y., W.-Y.C., and S.T. conducted the experiments. J.-M.Y., W.-Y.C., J.L., and C.-H.H. analyzed the data. W.-Y.C. developed deep learning models. P.A.I. carried out computational model fitting and simulations. J.-M.Y. and C.-H.H. wrote the manuscript with inputs from W.-Y.C., J.L., S.T., and P.A.I. C.-H.H. and J.-M.Y. supervised the study.

### DECLARATION OF INTERESTS

The authors declare no competing interests.

Received: March 19, 2021  
 Revised: September 27, 2021  
 Accepted: November 3, 2021  
 Published: November 26, 2021



## SUPPORTING CITATIONS

The following references appear in the Supplemental Information: Bondeva et al. (2002); Chatila et al. (1989); Chen and Tan (1998); Elzi et al. (2001); Guzeloglu et al. (2004); Jimenez-Vargas et al. (2018); Meus et al. (2017); Rao et al. (2001); Sample et al. (2015).

## REFERENCES

- Abadi, M., Agarwal, A., Barham, P., Brevdo, E., Chen, Z., Citro, C., Corrado, G.S., Davis, A., Dean, J., Devin, M., et al. (2015). TensorFlow: Large-scale machine learning on heterogeneous systems. arXiv, arXiv:1603.04467.
- Ai, H.-W., Shaner, N.C., Cheng, Z., Tsien, R.Y., and Campbell, R.E. (2007). Exploration of new chromophore structures leads to the identification of improved blue fluorescent proteins. *Biochemistry* 46, 5904–5910.
- Amano, M., Nakayama, M., and Kaibuchi, K. (2010). Rho-kinase/ROCK: A key regulator of the cytoskeleton and cell polarity. *Cytoskeleton (Hoboken)* 67, 545–554.
- Aoki, K., Kumagai, Y., Sakurai, A., Komatsu, N., Fujita, Y., Shionyu, C., and Matsuda, M. (2013). Stochastic ERK activation induced by noise and cell-to-cell propagation regulates cell density-dependent proliferation. *Mol. Cell* 52, 529–540.
- Bondeva, T., Balla, A., Várnai, P., and Balla, T. (2002). Structural determinants of Ras-Raf interaction analyzed in live cells. *Mol. Biol. Cell* 13, 2323–2333.
- Chapnick, D.A., Bunker, E., Liu, X., and Old, W.M. (2019). Temporal metabolite, ion, and enzyme activity profiling using fluorescence microscopy and genetically encoded biosensors. In *High-Throughput Metabolomics: Methods and Protocols*, A. D'Alessandro, ed. (Springer New York), pp. 343–353.
- Chatila, T., Silverman, L., Miller, R., and Geha, R. (1989). Mechanisms of T cell activation by the calcium ionophore ionomycin. *J. Immunol.* 143, 1283–1289.
- Chen, Y.R., and Tan, T.H. (1998). Inhibition of the c-Jun N-terminal kinase (JNK) signaling pathway by curcumin. *Oncogene* 17, 173–178.
- Chen, T.-W., Wardill, T.J., Sun, Y., Pulver, S.R., Renninger, S.L., Baohan, A., Schreier, E.R., Kerr, R.A., Orger, M.B., Jayaraman, V., et al. (2013). Ultrasensitive fluorescent proteins for imaging neuronal activity. *Nature* 499, 295–300.
- Chernov, K.G., Redchuk, T.A., Omelina, E.S., and Verkhusha, V.V. (2017). Near-Infrared Fluorescent Proteins, Biosensors, and Optogenetic Tools Engineered from Phytochromes. *Chem. Rev.* 117, 6423–6446.
- Chollet, F. (2018). Keras: The Python Deep Learning Library (Astrophysics Source Code Library).
- Chu, J., Haynes, R.D., Corbel, S.Y., Li, P., González-González, E., Burg, J.S., Ataie, N.J., Lam, A.J., Cranfill, P.J., Baird, M.A., et al. (2014). Non-invasive intravital imaging of cellular differentiation with a bright red-excitable fluorescent protein. *Nat. Methods* 11, 572–578.
- De Simone, A., Evanitsky, M.N., Hayden, L., Cox, B.D., Wang, J., Tornini, V.A., Ou, J., Chao, A., Poss, K.D., and Di Talia, S. (2021). Control of osteoblast regeneration by a train of Erk activity waves. *Nature* 590, 129–133.
- Elzi, D.J., Bjornsen, A.J., MacKenzie, T., Wyman, T.H., and Sillman, C.C. (2001). Ionomycin causes activation of p38 and p42/44 mitogen-activated protein kinases in human neutrophils. *Am. J. Physiol. Cell Physiol.* 281, C350–C360.
- Fosbrink, M., Aye-Han, N.-N., Cheong, R., Levchenko, A., and Zhang, J. (2010). Visualization of JNK activity dynamics with a genetically encoded fluorescent biosensor. *Proc. Natl. Acad. Sci. USA* 107, 5459–5464.
- Frame, M.C., Patel, H., Serrels, B., Lietha, D., and Eck, M.J. (2010). The FERM domain: organizing the structure and function of FAK. *Nat. Rev. Mol. Cell Biol.* 11, 802–814.
- Fritz, R.D., Letzelter, M., Reimann, A., Martin, K., Fusco, L., Ritsma, L., Ponsioen, B., Fluri, E., Schulte-Merker, S., van Rheenen, J., and Pertz, O. (2013). A versatile toolkit to produce sensitive FRET biosensors to visualize signaling in time and space. *Sci. Signal.* 6, rs12.
- Fritz, R.D., Menshykau, D., Martin, K., Reimann, A., Pontelli, V., and Pertz, O. (2015). SrGAP2-Dependent Integration of Membrane Geometry and Slit-2-Dependent Robo-Repulsive Cues Regulates Fibroblast Contact Inhibition of Locomotion. *Dev. Cell* 35, 78–92.
- Fujita, Y., Komatsu, N., Matsuda, M., and Aoki, K. (2014). Fluorescence resonance energy transfer based quantitative analysis of feedforward and feedback loops in epidermal growth factor receptor signaling and the sensitivity to molecular targeting drugs. *FEBS J.* 281, 3177–3192.
- Fukushima, S., Matsuoka, S., and Ueda, M. (2019). Excitable dynamics of Ras triggers spontaneous symmetry breaking of PIP3 signaling in motile cells. *J. Cell Sci.* 132, jcs224121.
- Gelens, L., Anderson, G.A., and Ferrell, J.E., Jr. (2014). Spatial trigger waves: positive feedback gets you a long way. *Mol. Biol. Cell* 25, 3486–3493.
- Glorot, X., and Bengio, Y. (2010). Understanding the difficulty of training deep feedforward neural networks. *J. Mach. Learn. Res.* 9, 249–256.
- Grant, D.M., Zhang, W., McGhee, E.J., Bunney, T.D., Talbot, C.B., Kumar, S., Munro, I., Dunsby, C., Neil, M.A.A., Katan, M., and French, P.M. (2008). Multiplexed FRET to image multiple signaling events in live cells. *Biophys. J.* 95, L69–L71.
- Greenwald, E.C., Mehta, S., and Zhang, J. (2018). Genetically Encoded Fluorescent Biosensors Illuminate the Spatiotemporal Regulation of Signaling Networks. *Chem. Rev.* 118, 11707–11794.
- Guzeloglu, A., Subramaniam, P., Michel, F., and Thatcher, W.W. (2004). Interferon-tau induces degradation of prostaglandin H synthase-2 messenger RNA in bovine endometrial cells through a transcription-dependent mechanism. *Biol. Reprod.* 71, 170–176.
- Harvey, C.D., Ehrhardt, A.G., Cellurale, C., Zhong, H., Yasuda, R., Davis, R.J., and Svoboda, K. (2008). A genetically encoded fluorescent sensor of ERK activity. *Proc. Natl. Acad. Sci. USA* 105, 19264–19269.
- Hinton, G., Srivastava, N., and Swersky, K. (2012). Neural networks for machine learning lecture 6a overview of mini-batch gradient descent. [https://www.cs.toronto.edu/~tijmen/csc321/slides/lecture\\_slides\\_lec6.pdf](https://www.cs.toronto.edu/~tijmen/csc321/slides/lecture_slides_lec6.pdf).
- Hiratsuka, T., Fujita, Y., Naoki, H., Aoki, K., Kamioka, Y., and Matsuda, M. (2015). Intercellular propagation of extracellular signal-regulated kinase activation revealed by in vivo imaging of mouse skin. *eLife* 4, e05178.
- Hoeller, O., Gong, D., and Weiner, O.D. (2014). How to understand and outwit adaptation. *Dev. Cell* 28, 607–616.
- Huang, C.Y., and Ferrell, J.E., Jr. (1996). Ultrasensitivity in the mitogen-activated protein kinase cascade. *Proc. Natl. Acad. Sci. USA* 93, 10078–10083.
- Huang, C.-H., Tang, M., Shi, C., Iglesias, P.A., and Devreotes, P.N. (2013). An excitable signal integrator couples to an idling cytoskeletal oscillator to drive cell migration. *Nat. Cell Biol.* 15, 1307–1316.
- Iglesias, P.A., and Shi, C. (2014). Comparison of adaptation motifs: temporal, stochastic and spatial responses. *IET Syst. Biol.* 8, 268–281.
- Jimenez-Vargas, N.N., Pattison, L.A., Zhao, P., Lieu, T., Latorre, R., Jensen, D.D., Castro, J., Aurelio, L., Le, G.T., Flynn, B., et al. (2018). Protease-activated receptor-2 in endosomes signals persistent pain of irritable bowel syndrome. *Proc. Natl. Acad. Sci. USA* 115, E7438–E7447.
- Kingma, D.P., and Ba, J. (2014). Adam: A Method for Stochastic Optimization. arXiv, arXiv:1412.6980.
- Komatsu, N., Aoki, K., Yamada, M., Yukinaga, H., Fujita, Y., Kamioka, Y., and Matsuda, M. (2011). Development of an optimized backbone of FRET biosensors for kinases and GTPases. *Mol. Biol. Cell* 22, 4647–4656.
- Konagaya, Y., Terai, K., Hirao, Y., Takakura, K., Imajo, M., Kamioka, Y., Sasaoka, N., Kakizuka, A., Sumiyama, K., Asano, T., and Matsuda, M. (2017). A Highly Sensitive FRET Biosensor for AMPK Exhibits Heterogeneous AMPK Responses among Cells and Organs. *Cell Rep.* 21, 2628–2638.
- Kremers, G.-J., Hazelwood, K.L., Murphy, C.S., Davidson, M.W., and Piston, D.W. (2009). Photoconversion in orange and red fluorescent proteins. *Nat. Methods* 6, 355–358.
- Kuchenov, D., Laketa, V., Stein, F., Salopiata, F., Klingmüller, U., and Schultz, C. (2016). High-Content Imaging Platform for Profiling Intracellular Signaling Network Activity in Living Cells. *Cell Chem. Biol.* 23, 1550–1559.

- Kunkel, M.T., Ni, Q., Tsien, R.Y., Zhang, J., and Newton, A.C. (2005). Spatio-temporal dynamics of protein kinase B/Akt signaling revealed by a genetically encoded fluorescent reporter. *J. Biol. Chem.* **280**, 5581–5587.
- Lambert, T.J. (2019). FPbase: a community-editable fluorescent protein database. *Nat. Methods* **16**, 277–278.
- Li, C., Imanishi, A., Komatsu, N., Terai, K., Amano, M., Kaibuchi, K., and Matsuda, M. (2017). A FRET Biosensor for ROCK Based on a Consensus Substrate Sequence Identified by KISS Technology. *Cell Struct. Funct.* **42**, 1–13.
- Linghu, C., Johnson, S.L., Valdes, P.A., Shemesh, O.A., Park, W.M., Park, D., Piatkevich, K.D., Wassie, A.T., Liu, Y., An, B., et al. (2020). Spatial Multiplexing of Fluorescent Reporters for Imaging Signaling Network Dynamics. *Cell* **183**, 1682–1698.e24.
- Ma, W., Trusina, A., El-Samad, H., Lim, W.A., and Tang, C. (2009). Defining network topologies that can achieve biochemical adaptation. *Cell* **138**, 760–773.
- Machacek, M., Hodgson, L., Welch, C., Elliott, H., Pertz, O., Nalbant, P., Abell, A., Johnson, G.L., Hahn, K.M., and Danuser, G. (2009). Coordination of Rho GTPase activities during cell protrusion. *Nature* **461**, 99–103.
- Marston, D.J., Vilela, M., Huh, J., Ren, J., Azoitei, M.L., Glekas, G., Danuser, G., Sondek, J., and Hahn, K.M. (2020). Multiplexed GTPase and GEF biosensor imaging enables network connectivity analysis. *Nat. Chem. Biol.* **16**, 826–833.
- Martin, K., Reimann, A., Fritz, R.D., Ryu, H., Jeon, N.L., and Pertz, O. (2016). Spatio-temporal co-ordination of RhoA, Rac1 and Cdc42 activation during prototypical edge protrusion and retraction dynamics. *Sci. Rep.* **6**, 21901.
- Mehta, S., Aye-Han, N.-N., Ganesan, A., Oldach, L., Gorshkov, K., and Zhang, J. (2014). Calmodulin-controlled spatial decoding of oscillatory Ca<sup>2+</sup> signals by calcineurin. *eLife* **3**, e03765.
- Mehta, S., Zhang, Y., Roth, R.H., Zhang, J.-F., Mo, A., Tenner, B., Haganir, R.L., and Zhang, J. (2018). Single-fluorophore biosensors for sensitive and multiplexed detection of signalling activities. *Nat. Cell Biol.* **20**, 1215–1225.
- Meus, M.-A., Hertig, V., Villeneuve, L., Jasmin, J.-F., and Calderone, A. (2017). Nestin Expressed by Pre-Existing Cardiomyocytes Recapitulated in Part an Embryonic Phenotype; Suppressive Role of p38 MAPK. *J. Cell. Physiol.* **232**, 1717–1727.
- Micutkova, L., Hermann, M., Offerdinger, M., Hess, M.W., Matscheski, A., Pircher, H., Mück, C., Ebner, H.-L., Laich, A., Ferrando-May, E., et al. (2012). Analysis of the cellular uptake and nuclear delivery of insulin-like growth factor binding protein-3 in human osteosarcoma cells. *Int. J. Cancer* **130**, 1544–1557.
- Miyamoto, T., Rho, E., Sample, V., Akano, H., Magari, M., Ueno, T., Gorshkov, K., Chen, M., Tokumitsu, H., Zhang, J., and Inoue, T. (2015). Compartmentalized AMPK signaling illuminated by genetically encoded molecular sensors and actuators. *Cell Rep.* **11**, 657–670.
- Newman, R.H., Fosbrink, M.D., and Zhang, J. (2011). Genetically encodable fluorescent biosensors for tracking signaling dynamics in living cells. *Chem. Rev.* **111**, 3614–3666.
- Ouyang, M., Sun, J., Chien, S., and Wang, Y. (2008). Determination of hierarchical relationship of Src and Rac at subcellular locations with FRET biosensors. *Proc. Natl. Acad. Sci. USA* **105**, 14353–14358.
- Pargett, M., Gillies, T.E., Teragawa, C.K., Sparta, B., and Albeck, J.G. (2017). Single-Cell Imaging of ERK Signaling Using Fluorescent Biosensors. *Methods Mol. Biol.* **1636**, 35–59.
- Piatkevich, K.D., Hult, J., Subach, O.M., Wu, B., Abdulla, A., Segall, J.E., and Verkhusha, V.V. (2010). Monomeric red fluorescent proteins with a large Stokes shift. *Proc. Natl. Acad. Sci. USA* **107**, 5369–5374.
- Rao, J.N., Li, L., Golovina, V.A., Platoshyn, O., Strauch, E.D., Yuan, J.X., and Wang, J.Y. (2001). Ca<sup>2+</sup>-RhoA signaling pathway required for polyamine-dependent intestinal epithelial cell migration. *Am. J. Physiol. Cell Physiol.* **280**, C993–C1007.
- Regot, S., Hughey, J.J., Bajar, B.T., Carrasco, S., and Covert, M.W. (2014). High-sensitivity measurements of multiple kinase activities in live single cells. *Cell* **157**, 1724–1734.
- Riedl, J., Crevenna, A.H., Kessenbrock, K., Yu, J.H., Neukirchen, D., Bista, M., Bradke, F., Jenne, D., Holak, T.A., Werb, Z., et al. (2008). Lifeact: a versatile marker to visualize F-actin. *Nat. Methods* **5**, 605–607.
- Sample, V., Ramamurthy, S., Gorshkov, K., Ronnett, G.V., and Zhang, J. (2015). Polarized activities of AMPK and BRSK in primary hippocampal neurons. *Mol. Biol. Cell* **26**, 1935–1946.
- Schindelin, J., Arganda-Carreras, I., Frise, E., Kaynig, V., Longair, M., Pietzsch, T., Preibisch, S., Rueden, C., Saalfeld, S., Schmid, B., et al. (2012). Fiji: an open-source platform for biological-image analysis. *Nat. Methods* **9**, 676–682.
- Schneider, C.A., Rasband, W.S., and Eliceiri, K.W. (2012). NIH Image to ImageJ: 25 years of image analysis. *Nat. Methods* **9**, 671–675.
- Seong, J., Ouyang, M., Kim, T., Sun, J., Wen, P.-C., Lu, S., Zhuo, Y., Llewellyn, N.M., Schlaepfer, D.D., Guan, J.-L., et al. (2011). Detection of focal adhesion kinase activation at membrane microdomains by fluorescence resonance energy transfer. *Nat. Commun.* **2**, 406.
- Shaner, N.C., Campbell, R.E., Steinbach, P.A., Giepmans, B.N.G., Palmer, A.E., and Tsien, R.Y. (2004). Improved monomeric red, orange and yellow fluorescent proteins derived from *Discosoma* sp. red fluorescent protein. *Nat. Biotechnol.* **22**, 1567–1572.
- Shaner, N.C., Lin, M.Z., McKeown, M.R., Steinbach, P.A., Hazelwood, K.L., Davidson, M.W., and Tsien, R.Y. (2008). Improving the photostability of bright monomeric orange and red fluorescent proteins. *Nat. Methods* **5**, 545–551.
- Shcherbakova, D.M., and Verkhusha, V.V. (2013). Near-infrared fluorescent proteins for multicolor in vivo imaging. *Nat. Methods* **10**, 751–754.
- Shen, Y., Chen, Y., Wu, J., Shaner, N.C., and Campbell, R.E. (2017). Engineering of mCherry variants with long Stokes shift, red-shifted fluorescence, and low cytotoxicity. *PLoS ONE* **12**, e0171257.
- Shindo, Y., Iwamoto, K., Mouri, K., Hibino, K., Tomita, M., Kosako, H., Sako, Y., and Takahashi, K. (2016). Conversion of graded phosphorylation into switch-like nuclear translocation via autoregulatory mechanisms in ERK signalling. *Nat. Commun.* **7**, 10485.
- Srivastava, N., Hinton, G., Krizhevsky, A., Sutskever, I., and Salakhutdinov, R. (2014). Dropout: A Simple Way to Prevent Neural Networks from Overfitting. *J. Mach. Learn. Res.* **15**, 1929–1958.
- Takaya, A., Kamio, T., Masuda, M., Mochizuki, N., Sawa, H., Sato, M., Nagashima, K., Mizutani, A., Matsuno, A., Kiyokawa, E., and Matsuda, M. (2007). R-Ras regulates exocytosis by Rgl2/Rlf-mediated activation of RalA on endosomes. *Mol. Biol. Cell* **18**, 1850–1860.
- Terai, K., and Matsuda, M. (2005). Ras binding opens c-Raf to expose the docking site for mitogen-activated protein kinase kinase. *EMBO Rep.* **6**, 251–255.
- Terai, K., and Matsuda, M. (2006). The amino-terminal B-Raf-specific region mediates calcium-dependent homo- and hetero-dimerization of Raf. *EMBO J.* **25**, 3556–3564.
- Terai, K., Imanishi, A., Li, C., and Matsuda, M. (2019). Two decades of genetically encoded biosensors based on Förster resonance energy transfer. *Cell Struct. Funct.* **44**, 153–169.
- Tsai, F.-C., Seki, A., Yang, H.W., Hayer, A., Carrasco, S., Malmersjö, S., and Meyer, T. (2014). A polarized Ca<sup>2+</sup>, diacylglycerol and STIM1 signalling system regulates directed cell migration. *Nat. Cell Biol.* **16**, 133–144.
- Tsou, P., Zheng, B., Hsu, C.-H., Sasaki, A.T., and Cantley, L.C. (2011). A fluorescent reporter of AMPK activity and cellular energy stress. *Cell Metab.* **13**, 476–486.
- Tu, Y., and Rappel, W.J. (2018). Adaptation in Living Systems. *Annu. Rev. Condens. Matter Phys.* **9**, 183–205.
- van Haastert, P.J.M., Keizer-Gunnink, I., and Kortholt, A. (2017). Coupled excitable Ras and F-actin activation mediates spontaneous pseudopod formation and directed cell movement. *Mol. Biol. Cell* **28**, 922–934.
- van Unen, J., Stumpf, A.D., Schmid, B., Reinhard, N.R., Hordijk, P.L., Hoffmann, C., Gadella, T.W.J., Jr., and Goedhart, J. (2016). A New Generation of FRET Sensors for Robust Measurement of G $\alpha$ 1, G $\alpha$ 2 and G $\alpha$ 3 Activation Kinetics in Single Cells. *PLoS ONE* **11**, e0146789.

- Violin, J.D., Zhang, J., Tsien, R.Y., and Newton, A.C. (2003). A genetically encoded fluorescent reporter reveals oscillatory phosphorylation by protein kinase C. *J. Cell Biol.* *161*, 899–909.
- Watton, S.J., and Downward, J. (1999). Akt/PKB localisation and 3' phosphoinositide generation at sites of epithelial cell-matrix and cell-cell interaction. *Curr. Biol.* *9*, 433–436.
- Welch, C.M., Elliott, H., Danuser, G., and Hahn, K.M. (2011). Imaging the coordination of multiple signalling activities in living cells. *Nat. Rev. Mol. Cell Biol.* *12*, 749–756.
- Xiang, X., Sun, J., Wu, J., He, H.-T., Wang, Y., and Zhu, C. (2011). A FRET-Based Biosensor for Imaging SYK Activities in Living Cells. *Cell. Mol. Bioeng.* *4*, 670–677.
- Xiong, Y., Huang, C.-H., Iglesias, P.A., and Devreotes, P.N. (2010). Cells navigate with a local-excitation, global-inhibition-biased excitable network. *Proc. Natl. Acad. Sci. USA* *107*, 17079–17086.
- Yang, H.W., Collins, S.R., and Meyer, T. (2016). Locally excitable Cdc42 signals steer cells during chemotaxis. *Nat. Cell Biol.* *18*, 191–201.
- Yang, J.-M., Bhattacharya, S., West-Foyle, H., Hung, C.-F., Wu, T.-C., Iglesias, P.A., and Huang, C.-H. (2018). Integrating chemical and mechanical signals through dynamic coupling between cellular protrusions and pulsed ERK activation. *Nat. Commun.* *9*, 4673.
- Zhan, H., Bhattacharya, S., Cai, H., Iglesias, P.A., Huang, C.-H., and Devreotes, P.N. (2020). An Excitable Ras/PI3K/ERK Signaling Network Controls Migration and Oncogenic Transformation in Epithelial Cells. *Dev. Cell* *54*, 608–623.e5.
- Zhang, J., Campbell, R.E., Ting, A.Y., and Tsien, R.Y. (2002). Creating new fluorescent probes for cell biology. *Nat. Rev. Mol. Cell Biol.* *3*, 906–918.
- Zhou, X., Clister, T.L., Lowry, P.R., Seldin, M.M., Wong, G.W., and Zhang, J. (2015). Dynamic Visualization of mTORC1 Activity in Living Cells. *Cell Rep.* *10*, 1767–1777.

## STAR★METHODS

### KEY RESOURCES TABLE

REAGENT or RESOURCE	SOURCE	IDENTIFIER
<b>Antibodies</b>		
p44/42 MAP kinase (phosphorylated Erk1/2) antibody	Cell Signaling	Cat# 9101, RRID:AB_331646
Phospho-FAK (Tyr397) (D20B1) Rabbit mAb antibody	Cell Signaling	Cat# 8556, RRID:AB_10891442
Rabbit Anti-GAPDH Monoclonal Antibody, Unconjugated, Clone 14C10	Cell Signaling	Cat# 2118, RRID:AB_561053
<b>Chemicals, peptides, and recombinant proteins</b>		
Phorbol-12,13-dibutyrate (PDBu)	EMD Millipore	#524390
Anisomycin	Sigma-Aldrich	A9789
UK14304	Sigma-Aldrich	U104
Yohimbine	Sigma-Aldrich	Y3125
Gefitinib	Cayman	#13166
Ionomycin	Peptidech	#5608212
Jasplakinolide	Cayman	#11705
Latrunculin B	Enzo Life Sciences	BML-T110-0001
PF562271	AdipoGen	SYN-1064
ZSTK474	Cell Signaling	#13213
Dasatinib	Cayman	#11498
GDC-0994	APEX BIO Technology	B5817
LY2584702	Selleck	S7698
BAPTA-AM	Selleck	S7534
Y27632	Enzo Life Sciences	ALX-270-333
EGF	Sigma-Aldrich	E9644
2-Deoxyglucose (2-DG)	Sigma-Aldrich	D8375
<b>Experimental models: Cell lines</b>		
Human: A6L	L. Wood Lab (JHU)	N/A
Human: HEK293T	C. Hung Lab (JHU)	N/A
Human: HeLa	M. Iijima Lab (JHU)	N/A
Human: MCF7	C. Hung Lab (JHU)	N/A
Human: SiHa	C. Hung Lab (JHU)	N/A
Human: U2OS	ATCC	HTB-96
Human: U87MG	M. Iijima Lab (JHU)	N/A
<b>Oligonucleotides</b>		
Primer for ERKKTR (forward): CAAgtcgac ATGAAGGGCCGAAAGCCTC	This paper	N/A
Primer for ERKKTR (reverse): CAAggatc cccGGATGGGAATTGAAAGCTGGACT	This paper	N/A
Primer for p38KTR (forward): CAActcgag ATGCGTAAGCCAGATCTCCG	This paper	N/A
Primer for p38KTR (reverse): CAAggatcccc GCTGGACTGGAGGGTCAG	This paper	N/A
Primer for JNKKTR (forward): CAActcgagA TGAGTAACCCTAAGATCCTAAAACAGAG	This paper	N/A
Primer for JNKKTR (reverse): CAAggatcccc GCTGGACTGGAGGGTCAG	This paper	N/A

(Continued on next page)



**Continued**

REAGENT or RESOURCE	SOURCE	IDENTIFIER
<b>Recombinant DNA</b>		
AMPKAR	<a href="#">Tsou et al., 2011</a>	Addgene plasmid #35097
AMPKAR-EV	<a href="#">Konagaya et al., 2017</a>	Addgene plasmid #105241
cyto-ABKAR	<a href="#">Miyamoto et al., 2015</a>	Addgene plasmid #61510
LAMP1-ABKAR	<a href="#">Miyamoto et al., 2015</a>	Addgene plasmid #65068
CaNAR2	<a href="#">Mehta et al., 2014</a>	Addgene plasmid #64728
ER-CaNAR2	<a href="#">Mehta et al., 2014</a>	Addgene plasmid #64732
PM-CaNAR2	<a href="#">Mehta et al., 2014</a>	Addgene plasmid #64730
GCaMP6S	<a href="#">Chen et al., 2013</a>	Addgene plasmid #40753
GCaMP6S-PM	<a href="#">Tsai et al., 2014</a>	Addgene plasmid #52228
EKAR	<a href="#">Harvey et al., 2008</a>	Addgene plasmid #18679
Nuc-EKAR	<a href="#">Harvey et al., 2008</a>	Addgene plasmid #18681
Lyn-EKAR	This paper	N/A
ERKKTR	<a href="#">Regot et al., 2014</a>	Addgene plasmid #59150
Cyto-FAK	<a href="#">Seong et al., 2011</a>	Addgene plasmid #78300
Lyn-FAK	<a href="#">Seong et al., 2011</a>	Addgene plasmid #78299
Src	<a href="#">Ouyang et al., 2008</a>	Addgene plasmid #78302
Gzi1	<a href="#">van Unen et al., 2016</a>	Addgene plasmid #69623
Gzi2	<a href="#">van Unen et al., 2016</a>	Addgene plasmid #69624
Gzi3	<a href="#">van Unen et al., 2016</a>	Addgene plasmid #69625
JNKAR	<a href="#">Fosbrink et al., 2010</a>	Addgene plasmid #61625
JNKKTR	<a href="#">Regot et al., 2014</a>	Addgene plasmid #59151
p38KTR	<a href="#">Regot et al., 2014</a>	Addgene plasmid #59152
PH-AKT	<a href="#">Watton and Downward, 1999</a>	N/A
AKTAR2	<a href="#">Zhou et al., 2015</a>	Addgene plasmid #64932
CKAR	<a href="#">Violin et al., 2003</a>	Addgene plasmid #14860
PM-CKAR	<a href="#">Violin et al., 2003</a>	Addgene plasmid #14862
RhoA-2G	<a href="#">Fritz et al., 2013</a>	Addgene plasmid #40176
Rac1-2G	<a href="#">Fritz et al., 2015</a>	Addgene plasmid #66110
Cdc42-2G	<a href="#">Martin et al., 2016</a>	Addgene plasmid #68814
LifeAct	<a href="#">Riedl et al., 2008</a>	Addgene plasmid #54610
Raichu-HRas	<a href="#">Komatsu et al., 2011</a>	N/A
Raichu-KRas	<a href="#">Komatsu et al., 2011</a>	N/A
Raichu-Rras	<a href="#">Takaya et al., 2007</a>	N/A
BKAR	<a href="#">Kunkel et al., 2005</a>	Addgene plasmid #14875
TORCAR	<a href="#">Zhou et al., 2015</a>	Addgene plasmid #64927
Prin-BRaf	<a href="#">Terai and Matsuda, 2006</a>	N/A
Prin-CRAF	<a href="#">Terai and Matsuda, 2005</a>	N/A
EV-RSK	<a href="#">Komatsu et al., 2011</a>	N/A
EV-ROCK	<a href="#">Li et al., 2017</a>	N/A
EV-S6K	<a href="#">Komatsu et al., 2011</a>	N/A
EV-EGFR (PicchuEV(CrklI))	<a href="#">Komatsu et al., 2011</a>	N/A
Syk biosensor	<a href="#">Xiang et al., 2011</a>	Addgene plasmid #125729
pEGFP-N1	CloneTech	N/A
EBFP2-Nucleus-7	gift from Michael Davidson	Addgene plasmid #55249
H2B-TagRFP	gift from Philipp Keller	Addgene plasmid #99271
pmCherry-NLS	<a href="#">Micutkova et al., 2012</a>	Addgene #39319
mCardinal-H2B-C-10	<a href="#">Chu et al., 2014</a>	Addgene plasmid #56162

(Continued on next page)

**Continued**

REAGENT or RESOURCE	SOURCE	IDENTIFIER
mCardinal-N1	Chu et al., 2014	Addgene #54590
piRFP702-N1	Shcherbakova and Verkhusha, 2013	Addgene plasmid #45456
piRFP682-N1	Shcherbakova and Verkhusha, 2013	Addgene plasmid #45459
pNLS-iRFP670	Shcherbakova and Verkhusha, 2013	Addgene plasmid #45466
mNeptune2-C1	gift from Michael Davidson	Addgene plasmid #54836
mNeptune2.5	Chu et al., 2014	Addgene plasmid #51310
mPlum-C1	Kremers et al., 2009	Addgene plasmid #54839
RDSmCherry1	Shen et al., 2017	Addgene plasmid #89987
LSS-mKate2-C1	Piatkevich et al., 2010	Addgene plasmid #31869
mStrawberry-N1	Shaner et al., 2004	Addgene #54644
pDONR221	Invitrogen	#12536017
pLex307	gift from David Root	Addgene plasmid #41392
pMD2.G	gift from Didier Trono	Addgene plasmid #12259
psPAX2	gift from Didier Trono	Addgene plasmid #12260

**Software and algorithms**

Zen Microscopy Software	Zeiss	<a href="https://www.zeiss.com/microscopy/us/products/microscope-software/zen.html">https://www.zeiss.com/microscopy/us/products/microscope-software/zen.html</a>
ImageJ/Fiji	Schindelin et al., 2012; Schneider et al., 2012	<a href="https://imagej.nih.gov/ij/">https://imagej.nih.gov/ij/</a>
Python	Python Software Foundation	<a href="https://www.python.org">https://www.python.org</a>
Keras	Chollet, 2018	<a href="https://keras.io/">https://keras.io/</a>
TensorFlow	Abadi et al., 2015	<a href="https://www.tensorflow.org/">https://www.tensorflow.org/</a>
Dropout	Srivastava et al., 2014	N/A
RMSprop	Hinton et al., 2012	N/A
Adam	Kingma and Ba, 2014	N/A
Glorot Initializer	Glorot and Bengio, 2010	N/A
MATLAB	MathWorks	<a href="https://www.mathworks.com/products/matlab.html">https://www.mathworks.com/products/matlab.html</a>

**RESOURCE AVAILABILITY**

**Lead contact**

Further information and requests for resources and reagents should be directed to and will be fulfilled by the Lead Contact Chuan-Hsiang Huang ([chaung29@jhmi.edu](mailto:chaung29@jhmi.edu)).

**Materials availability**

Plasmids generated in this study will be deposited to Addgene (<https://www.addgene.org>).

**Data and code availability**

All data supporting the findings of the current study are available within the article and its Supplemental Information files or from the corresponding authors upon reasonable request. The codes used in the study are provided as a ZIP file (Data S1).

**EXPERIMENTAL MODEL AND SUBJECT DETAILS**

HeLa, HEK293T, MCF7, and U2OS cells, purchased from ATCC, were grown at 37°C and 5% CO<sub>2</sub> in DMEM high glucose medium (GIBCO, #11965092) supplemented with 10% FBS (Corning Cellgro, 35-010-CV), 1 mM sodium pyruvate (GIBCO, #11360070), and 1X nonessential amino acids (GIBCO, #11140076). Transient transfections were performed using GenJet *In Vitro* DNA Transfection Reagent ver. II (SignaGen, #SL100499), GenJet *In Vitro* DNA Transfection Reagent for MCF7 cells (SignaGen, #SL100489-MCF7), or GenJet *In Vitro* DNA Transfection Reagent for U2OS cells (SignaGen, #SL100489-OS) following the manufacturer's instructions. For biosensor barcoding, 2x10<sup>5</sup> cells were seeded in 12-well plates and allowed to attach overnight. Cells in each well were transfected

with a pair of barcoding proteins and one biosensor, using a total of 0.75  $\mu\text{g}$  plasmid per well. The next day, cells were harvested from each well with Accutase (Corning, 25-058-CI) and mixed together. The resulting cell mixture was then seeded into 35 mm glass-bottom dishes (Mattek, P35GC-0-14-C) at  $7 \times 10^5$  cells per dish and incubated at  $37^\circ\text{C}$  and 5%  $\text{CO}_2$  overnight. The cells were starved in serum-free, phenol red-free DMEM (GIBCO, #21063029) for 1 h before imaging experiments.

## METHOD DETAILS

### Plasmids

#### Biosensors

Plasmids for biosensors were purchased from Addgene (see [Table S1](#)). ERKKTR, p38KTR and JNKKTR genes were further cloned into pEGFP-N1 (CloneTech) via XhoI/SalI and BamHI restriction sites using the following primers:

5'-CAAgtcgacATGAAGGGCCGAAAGCCTC-3' and 5'-CAAagatccccGGATGGGAATTGAAAGCTGGACT-3' for ERKKTR, 5'-CAA;ctcgagATGCGTAAGCCAGATCTCCG-3' and 5'-CAAagatccccGCTGGACTGGAGGGTCAG-3' for p38KTR; 5'-CAAactcgagATGAGT AACCTAAGATCCTAAAACAGAG-3' and 5'-CAAagatccccGCTGGACTGGAGGGTCAG-3' for JNKKTR.

#### Barcoding proteins

The original set of barcoding proteins were derived from five fluorescent proteins (designated A: TagRFP, B: mCardinal, C: iRFP702, D: BFP, and E: mCherry) linked to targeting sequences of four subcellular locations (designated 1: nucleus, 2: plasma membrane, 3: nuclear membrane, and 4: cytoplasm). Thus, a total of 16 barcoding proteins were generated, each represented by a letter-number combination (e.g., B1 indicates mCardinal targeted to the nucleus). To construct barcoding proteins, the following fragments were joined together by overlapping PCR: 1) fluorescent protein sequence; 2) spacer (TCTGGCAGCGGAGGCTCTGGAGGC); and 3) targeting sequence. The following plasmids were used as templates for the fluorescent proteins: H2B-TagRFP (Addgene #99271, a gift from Philipp Keller), mCardinal-H2B-C-10 (Addgene #56162) ([Chu et al., 2014](#)), piRFP702-N1 (Addgene #45456) ([Shcherbakova and Verkhusha, 2013](#)), EBFP2-Nucleus-7 (Addgene #55249, a gift from Michael Davidson), and pmCherry-NLS (Addgene #39319) ([Micutkova et al., 2012](#)). The targeting sequences for the nucleus, plasma membrane, nuclear membrane, and cytoplasm were derived from the NLS of SV40, CAAX of K-Ras, lamin B1, and the NES of MAPKK, respectively. The sequence ATGGGATGTATAAAATC AAAAGGGAAAGACAGC, derived from the Lyn kinase, was used as an alternative plasma membrane targeting motif in some cells. Additional fluorophores used for further expanding the barcoding proteins are shown in [Table S4](#).

### Chemical reagents

Stocks of 200  $\mu\text{M}$  phorbol-12,13-dibutyrate (PDBu, EMD Millipore, #524390), 1 mg/mL anisomycin (Sigma-Aldrich, A9789), 10 mM UK14304 (Sigma-Aldrich, U104), 10 mM yohimbine (Sigma-Aldrich, Y3125), 1 mM gefitinib (Cayman, #13166), 1 mM ionomycin (Peptide, #5608212), 2 mM jasplakinolide (Cayman, #11705), 25 mM latrunculin B (Enzo Life Sciences, BML-T110-0001), 10 mM PF562271 (AdipoGen, SYN-1064), 10 mM ZSTK474 (Cell Signaling, #13213), 10 mM dasatinib (Cayman, #11498), 10 mM GDC-0994 (APEXIO Technology, B5817), 1 mM LY2584702 (Selleck, S7698), 10 mM BAPTA-AM (Selleck, S7534) were prepared by dissolving the chemicals in DMSO; 10 mM Y27632 (Enzo Life Sciences, #ALX-270-333) in water. Stocks were diluted to the indicated final concentrations in the culture medium. The EGF stock solution was prepared by dissolving EGF (Sigma-Aldrich, E9644) in 10 mM acetic acid to a final concentration of 1 mg/ml. All drug stocks were stored at  $-20^\circ\text{C}$ . 2-Deoxyglucose (2-DG, MilliporeSigma, #D8375) was dissolved in culture medium to 100 mM and used immediately.

### Lentivirus production and transduction

Lentiviral plasmids were constructed using the Gateway Recombination Cloning Technology ([Figure S3](#)). Entry vectors were generated by integrating targeting sequence into pDONR221 (Invitrogen, #12536017) with Gateway BP Clonase II Enzyme Mix (Invitrogen, #11789100). To generate fluorescent protein sequence-inserted destination vectors, the upstream sequence of the attR1 sequence of pLex307 (Addgene, #41392) was first modified from 5'-GCTAGCATCGATTGATCA-3' to 5'-GCTAGCTTAATTAAGGGCATATGATCGATGGATCA-3' to insert PacI and NheI restriction enzyme sites and to remove an in-frame stop codon in the BclI restriction enzyme site. The fluorescent protein sequence was subsequently cloned into the vector via PacI and NheI sites. The final expression vectors were generated by transferring the targeting sequence from the entry vector to the destination vector with Gateway LR Clonase II Enzyme Mix (Invitrogen, #11791100).

For lentivirus production,  $4 \times 10^6$  HEK293T were seeded in a 10-cm dish with DMEM supplemented with 10% FBS and allowed to attach overnight. Cells were transfected with 1.25  $\mu\text{g}$  of pMD2.G (Addgene, #12259), 3.75  $\mu\text{g}$  of psPAX2 (Addgene, #12260), and 5  $\mu\text{g}$  of lentiviral plasmids using GenJet *In Vitro* DNA Transfection Reagent ver. II, and the cell culture medium was replaced with fresh medium 5 h after transfection. Lentiviral supernatants were harvested 24 h after transfection and filtered through a 0.45  $\mu\text{m}$  PVDF filter (Millipore, #SLHVM33RS).

For lentiviral transduction of U87MG, SiHa, and A6L, cells were seeded into an 8-well chamber ( $2.5 \times 10^4$  cells) with DMEM supplemented with 10% FBS and allowed to attach overnight. Cells were transduced with lentivirus in medium containing 8  $\mu\text{g}/\text{ml}$  polybrene (Millipore, #TR-1003-G). Cells were incubated at  $37^\circ\text{C}$  and 5%  $\text{CO}_2$  for 48 h before imaging.

## Microscopy

Imaging experiments were carried out on a Zeiss LSM 780 or 880 single-point laser-scanning microscope (Zeiss AxioObserver with 780 or 880-Quasar confocal module; 34-channel spectral, high-sensitivity gallium arsenide phosphide (GaAsP) detectors) with a motorized stage for capturing multiple viewfields controlled by Zen software as previously described (Huang et al., 2013). Live-cell imaging was carried out in a temperature/humidity/CO<sub>2</sub>-regulated chamber. To image barcodes, spectral images for red-far red barcoding proteins were acquired between 560 and 695 nm at 8.9 nm windows using Lambda Mode under 561 nm and 633 nm illumination. Reference spectra for TagRFP, mCherry, mCardinal, and iRFP702 were acquired by imaging HeLa cells expressing H2B-TagRFP under 561 nm excitation, H2B-mCherry and H2B-mCardinal under both 561 and 633 nm excitation, and H2B-iRFP702 under 633 nm excitation. Since the BFP emission spectrum is well separated from those of the red-far red fluorophores (Figure 1A), no unmixing is required for BFP images, which were therefore acquired in the channel mode. To avoid bleedthrough from CFP and YFP used in FRET-based biosensors, we collected BFP emission in the 370–430 nm range under 405 nm excitation. To image biosensors, CFP (458–499 nm) and YFP (508–543 nm) emissions under 458 nm illumination were obtained. This setting, while optimized for detecting CFP-YFP FRET biosensors, also captures GFP-based biosensors due to the overlapping spectra of GFP and YFP. Using a single imaging setting for both types of biosensors is convenient, and it reduces cell exposure to illumination, therefore minimizing phototoxicity. Time-lapse images of the biosensors were taken at a rate of one frame every three minutes unless specified. Cells in 2 mL DMEM (GIBCO #21063029) were stimulated by adding signaling activators or inhibitors (200 μL for 2DG and 20 μL for all other reagents) at the indicated time points.

## Image analysis

### Analysis of barcodes by linear unmixing of spectral images

Using the linear unmixing function in ZEN Software, spectral images of cells expressing pairs of barcoding proteins acquired under 561 nm illumination were unmixed using TagRFP and mCardinal reference spectra, whereas spectral images acquired under 633 nm illumination were unmixed with mCardinal and iRFP702 spectra. The unmixed images for TagRFP, mCardinal, and iRFP702 as well as images of BFP were then combined using NIH ImageJ and Fiji (Schindelin et al., 2012; Schneider et al., 2012) and visually inspected for the expression and localization of each fluorophore. In the majority of cases (> 90%) the two expressed barcoding proteins could be unambiguously identified (Figure S1). Cells with ambiguous barcodes were excluded from the analysis of biosensors. For simplicity, barcodes were represented by four numbers that denoted the expression and location of TagRFP, mCardinal, iRFP702, and BFP (0: no expression; 1: nucleus; 2: plasma membrane, 3: nuclear membrane, and 4: cytoplasm; see Figure 1C). For the second barcoding scheme in which one of the three red FPs (mCherry, mCardinal, or iRFP702) was combined with BFP (Figure 3), spectral images acquired under 633 nm excitation were unmixed using the reference spectra of mCherry, mCardinal, and iRFP702 followed by processing in NIH ImageJ and Fiji as described above.

### Analysis of biosensors in mixed populations of barcoded cells

Images of biosensors were processed and analyzed with NIH ImageJ and Fiji (Schindelin et al., 2012; Schneider et al., 2012). The barcode of each cell, determined as described above, allows for identification of the biosensor expressed by the cell. To measure the activities of FRET-based biosensors, the mean intensity of YFP over the entire cell was divided by that of CFP for each frame. For ERKKTR, p38KTR and JNKKTR, the mean intensity of YFP in the nucleus was divided by that of a cytoplasmic region. For PH-AKT, the mean intensity of YFP in an intracellular region was measured. For GCaMP6S and GCaMP6S-PM, the mean intensity of YFP over the entire cell was measured. The activities for every frame were then normalized to the average of those from the pre-stimulus frames. Normalized activities from cells with the same barcode were then pooled together to calculate the mean and standard deviation (SD) for the corresponding biosensor.

## Barcode image classification by deep learning models

### Image datasets

To create training and testing sets for deep learning models, we manually segmented processed barcode images (see Image Analysis above) comprising four channels (BFP, mCherry, mCardinal, and iRFP702), two of which contained “real” signals of an FP targeted to one of four distinct subcellular locations (the nucleus, plasma membrane, nuclear membrane, or cytosol), in ImageJ (Schindelin et al., 2012). Low quality or ambiguous images were discarded. Images from channels that did not correspond to a barcoding protein were included in the “none” class, thus generating a total of five image classes. Since mCherry, mCardinal, and iRFP702 images were obtained by linear unmixing of spectral images (see above), they sometimes contained noise and bleedthrough signals from other channels. We therefore performed a “mutual exclusion” correction, whereby we compared the mCherry, mCardinal, and iRFP702 images pixelwise and set the pixels from the two lower intensity channels to 0. This is because after unmixing, the channel with the real signal generally had the highest intensity. We used a script created in Python (Python Software Foundation. Python Language Reference, version 3.7, <https://www.python.org>) to carry out “mutual exclusion” correction followed by rescaling the pixel values to be between 0 and 1 and resizing to 150 pixels by 150 pixels. The final dataset contained 8,946 images (2,000 nucleus, 1,304 plasma membrane, 819 nuclear membrane, 1,724 cytosol, and 3,099 none), which were split into training (6,516 images), validation (1,630 images), and test sets (800 images).

### Deep Convolutional Neural Network

We trained three deep convolutional neural network models using Keras (Chollet, 2018) with the TensorFlow (Abadi et al., 2015) backend: one model to classify BFP images and two models to classify red FP images with a known BFP reference marker. The model for



BFP image classification had six layers, including four convolutional layers and two fully connected layers. We used 32, 64, 128, and 128 for the number of units in the convolutional layers and 512 and 3 in the fully connected layers. The two networks for red FP image classification had seven layers, including four convolutional layers and three fully connected layers. We used 32, 64, 128, and 128 for the number of units in the convolutional layers and 512, 128 and 5 in the fully connected layers. We used  $3 \times 3$  convolutional filters for every convolutional layer and  $2 \times 2$  max pooling with step size 2 after every convolutional layer. For the activation function, we used rectified linear units for every layer except for the last layer, in which we used Softmax for the 3-class and 5-class classifiers. We included a Dropout (with a rate of 0.5) between the last convolutional layer and fully connected layer to prevent overfitting (Srivastava et al., 2014). We used the RMSprop (Hinton et al., 2012) or Adam (Kingma and Ba, 2014) (initial learning\_rate = 0.001, beta\_1 = 0.9, beta\_2 = 0.999) optimizer with a batch of 32 training images to minimize the cross-entropy loss. The weights were initialized with the default Glorot initializer provided by Keras (Glorot and Bengio, 2010). The maximum output of the softmax function was used for thresholding during the barcode identification analysis.

We used the preprocessed images as described above to train the BFP models. For the two red FP classification models, images from the red FP channels were combined with either nuclear or plasma membrane BFP images to form a two-channel image resized to 150 pixels x 150 pixels. Before inputting the images into the neural network, we augmented the training images (using ImageGenerator) by randomly shifting, shearing, horizontal/vertical flipping, or rotating the images. The models were trained for  $\sim 100$  epochs, selected according to validation loss, and subsequently tested on the test data.

### Fitting responses to kinetic models

Suppose that  $y_{(ij)}(t_k)$  denotes the normalized biosensor level for biosensor  $i$ , cell  $j$  at time  $t_k$ . These time-dependent traces were fit to a model:

$$\hat{y}(t) = \begin{cases} a_1, & x < t_0 \\ a_1 - a_2(1 - e^{-a_3(t-t_0)})e^{-a_4(t-t_0)}, & x \geq t_0 \end{cases}$$

in two different ways. In the first, one set of parameters  $a_1, \dots, a_4$  and  $t_0$  was selected to minimize the sum of all the (squared) differences between the  $\hat{y}(t_k)$  and all the traces; i.e.

$$\min_{a_1, \dots, a_4, t_0} \sum_j \sum_k (y_{(ij)}(t_k) - \hat{y}(t_k))^2$$

This was done for ten individual experiments. Furthermore, for each specific cell-biosensor pair, a set of coefficients was obtained that minimized

$$\min_{a_1, \dots, a_4, t_0} \sum_k (y_{(ij)}(t_k) - \hat{y}(t_k))^2$$

Minimization was carried out using nonlinear least-squares optimization in MATLAB (MathWorks, Natick, MA) using the “fit” command of the Curve Fitting Toolbox (version 2020b). Sample values are given in Figure S4.

### Simulation of RTK network responses to EGF stimulation

The experimental mean data from Figure 6D were fitted to one of three models, according to the respective classes. The first, a receptor/ligand binding model described by  $R + L \rightleftharpoons C$  is given by the differential equation

$$\frac{dC}{dt} = -k_1 C + \frac{k_2 L}{k_3 + L}, t \geq t_0 \quad (1)$$

The four parameters,  $k_1, k_2, k_3$  and  $t_0$ , were obtained by fitting the experimental data to the simulation using a custom-based script in MATLAB that relies on fminsearch for the nonlinear optimization and ode45 to solve for the differential equation. Here,  $L$  is the stimulus strength (0.1, 1, 10 and 100 ng/ml) and is the normalized activity of the biosensor (minus one, so that the prestimulus level is zero). This model was used to fit the experimental data for PicchuEV.

The second model represents the combined activity of a receptor model (as in Equation 1) and a negative feedback loop as follows:

$$\frac{dC}{dt} = -k_1 C + \frac{k_2 L}{k_3 + L}, t \geq t_0$$

$$\frac{dX}{dt} = -\frac{k_8 XY}{k_9 + X} + \frac{k_6 C(k_4 - X)}{k_7 + (k_4 - X)} \quad \frac{dY}{dt} = -\frac{k_{12} Y}{k_{13} + Y} + \frac{k_{10} X(k_5 - Y)}{k_{11} + (k_5 - Y)}$$

In this model, the two species, X and Y, exist in two states, and the transitions between the two states is mediated by Michaelis-Menten kinetics. The various parameters,  $k_1, \dots, k_{13}$  and  $t_0$ , were obtained as in the first model, fitting the level of X to the biosensor data. This model was used to describe Syk, Lyn-FAK, RhoA2G, SRC, EVROCK and EV-S6K.

The third model represents the combined activity of a receptor model (as in Equation 1) and an activator-inhibitor excitable network (Xiong et al., 2010):

$$\frac{dC}{dt} = -k_1 C + \frac{k_2 L}{k_3 + L}, t \geq t_0 \quad \frac{dU}{dt} = -(k_4 + k_5 V)U + \frac{k_6 U^2}{k_7^2 + U^2} + k_4 C \quad \frac{dV}{dt} = -k_9 V + k_{10} U$$

The various parameters,  $k_1, \dots, k_{10}$  and  $t_0$ , were obtained as in the previous model, fitting the level of U to the biosensor data. This model was used to fit the data for GCaMP6S, EKAR and PH-AKT.

The various parameter values are given in the following table. Note that, except for  $t_0$ , which is given in minutes, all other parameters are non-dimensional.

Biosensor	$t_0$	$k_1$	$k_2$	$k_3$	$k_4$	$k_5$	$k_6$	$k_7$	$k_8$	$k_9$	$k_{10}$	$k_{11}$	$k_{12}$	$k_{13}$
PicchuEV	8.338	0.368	0.134	2.251										
GCaMP6S	4.916	0.484	0.114	6.043	0.461	2.306	2.167	0.8560	1.3493	0.0960	0.1251			
EKAR	7.582	0.741	0.178	0.361	1.503	1.035	0.130	0.0341	0.0799	$2.24 \times 10^{-5}$	0.2741			
PH-AKT	3.497	0.973	0.108	0.335	0.691	0.456	0.40	0.1314	0.2136	$1.25 \times 10^{-12}$	0.6303			
EV-ROCK	5.609	2.007	0.190	3.550	0.110	1.566	0.628	0.070	0.040	$1.42 \times 10^{-4}$	1.440	$1.83 \times 10^{-9}$	0.071	0.079
EV-S6K	7.701	0.165	0.137	1.939	0.675	0.210	0.046	0.592	0.877	0.367	0.387	0.204	0.109	1.370
Lyn-FAK	5.967	4.817	0.647	18.29	0.241	0.054	6.171	2.300	1.891	$1.06 \times 10^{-6}$	4.235	7.158	$7.946 \times 10^{-3}$	0.159
RhoA2G	5.362	0.476	0.196	3.961	0.221	0.488	1.203	1.657	0.487	0.547	0.978	$8.44 \times 10^{-4}$	0.067	0.044
SRC	5.403	0.652	0.175	3.279	0.582	0.450	1.208	0.697	0.405	$3.38 \times 10^{-7}$	0.260	$7.01 \times 10^{-4}$	0.064	0.135
Syk	6.565	0.826	0.112	1.964	0.854	0.070	1.083	0.500	1.170	$2.49 \times 10^{-5}$	0.271	$5.20 \times 10^{-4}$	0.045	0.074

### Hill equation fitting

To perform fitting of the Hill equation, we took the peak values of the responses of each biosensor at four different concentrations (0.1, 1, 10, 100 ng/ml) of EGF stimulation, scaled it to the maximum response, and fitted it to

$$y = 1 / (1 + (K/x)^n)$$

where  $K$  is the concentration of half responses,  $x$  is the measurement, and  $n$  is the Hill coefficient. The fitting is performed with the `curve_fit` tool in the Python library “`scipy.optimize`” with nonlinear least-squares regression.

### QUANTIFICATION AND STATISTICAL ANALYSIS

Python and Microsoft Excel were used for statistical analysis and generating graphs. Specifically, Python Seaborn package was used for plotting Figures 5E and 5G and Python matplotlib.pyplot package for Figures 6C–6E. For imaging experiments involving mixed barcoded cells, at least three independent experiments were carried out on different days, and statistics were derived by aggregating the number of samples noted in each figure legend across independent experiments. Mean  $\pm$  SD was reported as indicated in the figure legends. Statistical significance and  $p$ -values for comparing the responses of single and mixed cell populations (Table S2) were determined using two-tailed unpaired Welch’s t test for comparison between the two groups.

# Supplemental figures

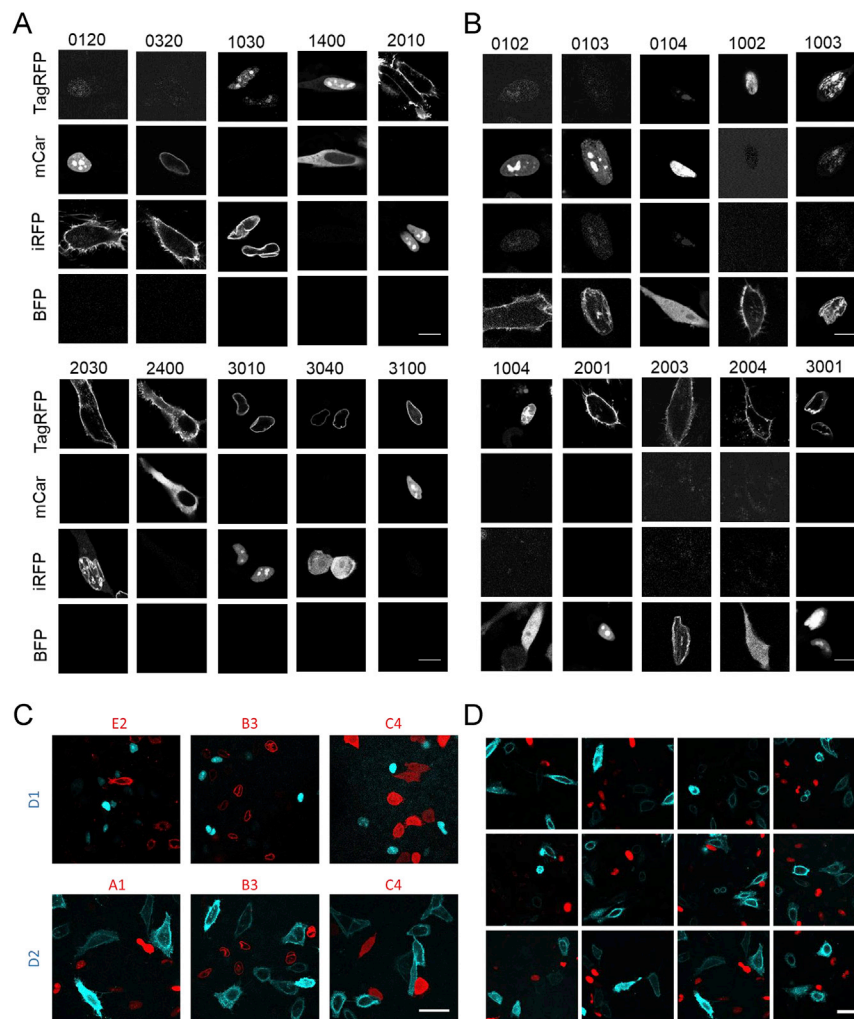


**Figure S1. Images of barcoded cells, related to Figure 1**

(A-B) Examples of HeLa cells expressing pairs of red/far-red barcoding proteins (A) and HeLa cells expressing BFP and one of the three red/far-red FPs (B). Spectral images of cells expressing pairs of barcoding proteins targeted to different subcellular locations were unmixed to obtain three images corresponding to TagRFP, mCardinal, and iRFP702, respectively. BFP was imaged separately. The numbers on top of every set of images denote barcodes as defined in Figure 1C legend. 20 out of 72 possible barcodes are shown. Scale bars: 10  $\mu\text{m}$ .

(C-D) Absence of cross-transfection in mixed barcoded cells. (C) Representative images of HeLa cells transfected with BFP targeted to the nucleus (D1) or plasma membrane (D2) mixed with cells transfected with one of the red FPs (A: TagRFP; B: mCardinal; C: iRFP702; E: mCherry) localized to different locations (1: nucleus; 2: cell membrane; 3: nuclear membrane; 4: cytosol). (D) Collage of 12 viewing fields from a single microscopy experiment showing HeLa cells transfected with plasma membrane-targeted BFP (cyan) mixed with cells transfected with nuclear TagRFP (red). Scale bars: 50  $\mu\text{m}$ .

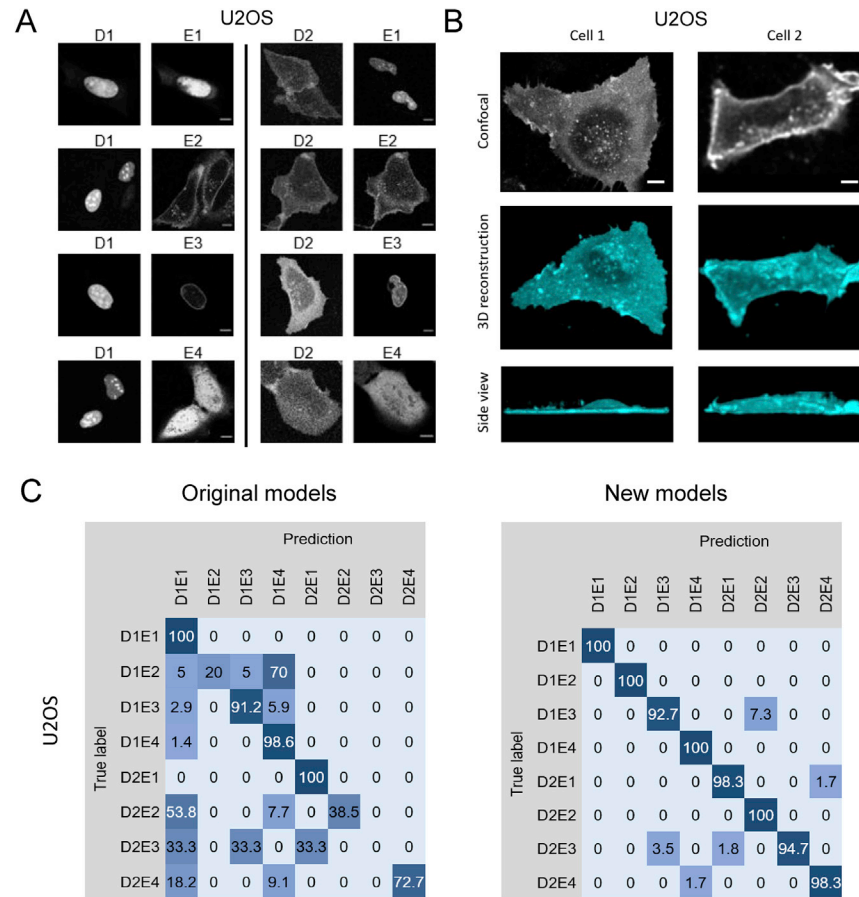


**Figure S2. Barcoding U2OS cells, related to Figure 4**

(A) Representative images of U2OS cells transfected with BFP targeted to the nucleus (D1) or plasma membrane (D2) along with mCherry targeted to one of the four subcellular locations (E1: nucleus; E2: plasma membrane; E3: nuclear membrane; E4: cytosol). Lyn sequence was used for plasma membrane targeting in U2OS cells. Scale bars: 10  $\mu\text{m}$ .

(B) 3D reconstruction from z-stacks of a U2OS cell with broad membrane signal of Lyn-CFP showing the "cowboy hat" morphology (left). A cell with sharply localized membrane signal (right) is shown for comparison. Scale bars: 10  $\mu\text{m}$ .

(C) Confusion matrix (%) of U2OS cells barcoded with nuclear or cytoplasmic BFP plus mCherry targeted to one of the four subcellular locations using the deep learning models trained on HeLa cells (original models, left) and new models trained on U2OS cell images (right).



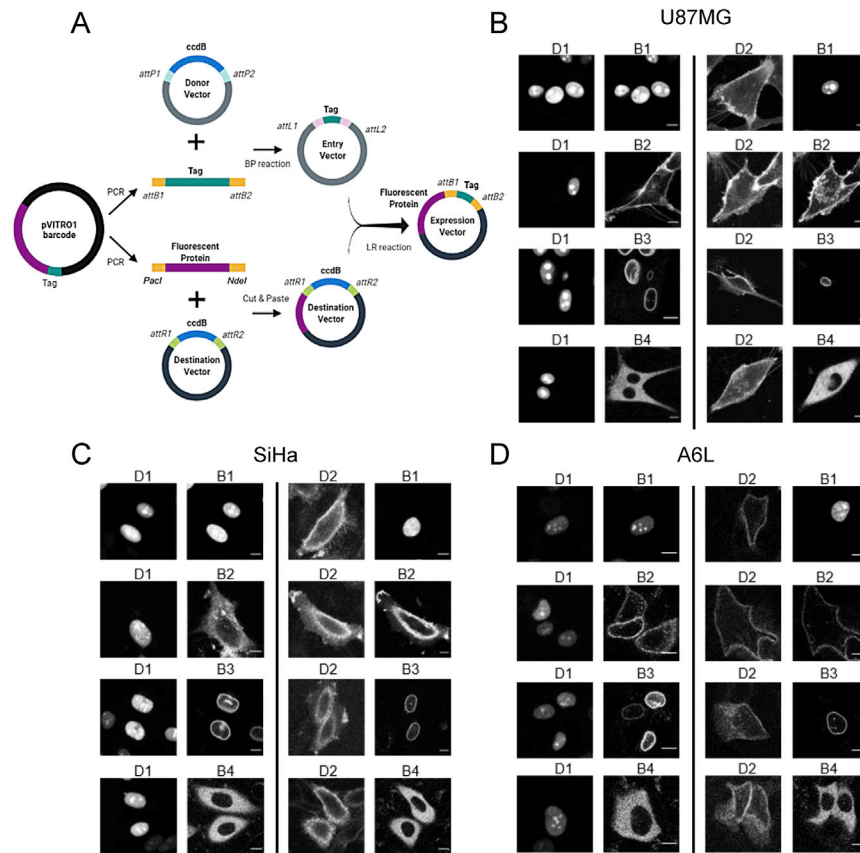


**Figure S3. Lentiviral vectors for barcoding, related to STAR Methods**

(A) Schematic of lentiviral vector construction.

(B-D) Representative images of U87MG (B), SiHa (C), and A6L (D) cells co-transduced with lentiviral vectors expressing BFP targeted to the nucleus (D1) or plasma membrane (D2) along with mCardinal targeted to one of the four subcellular locations (B1: nucleus; B2: plasma membrane; B3: nuclear membrane; B4: cytosol). Scale bars: 10 μm.

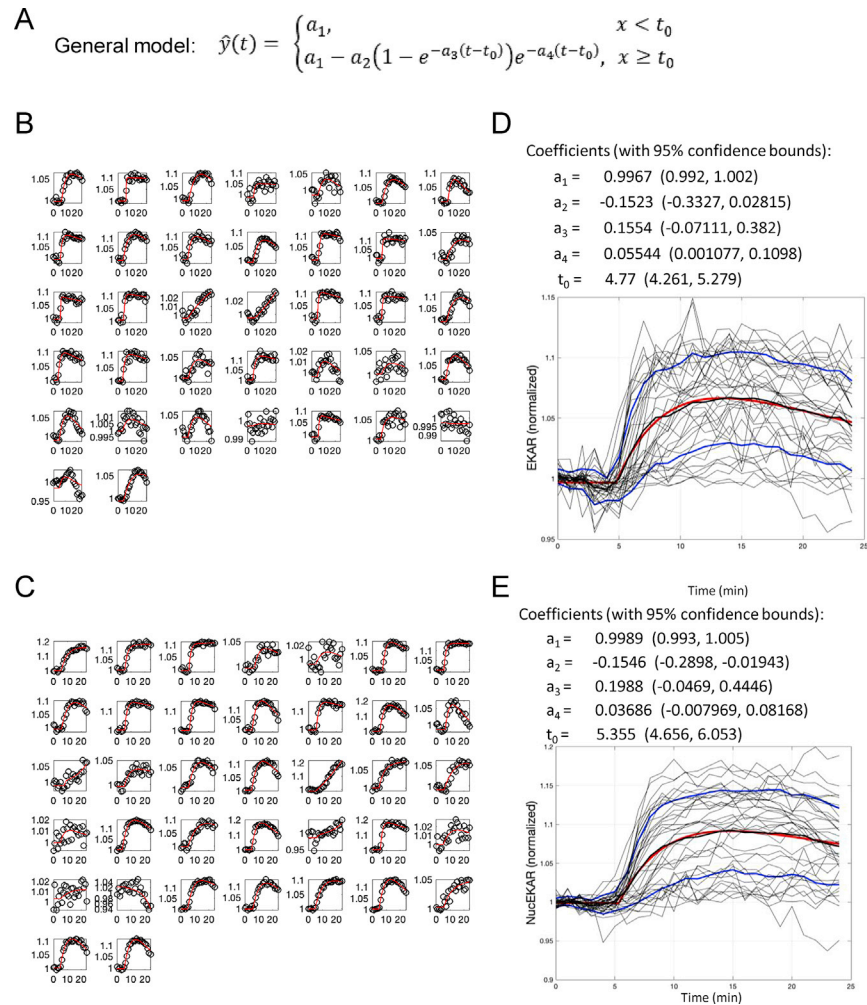


**Figure S4. Fitting responses to kinetic models, related to Figure 5 and STAR Methods**

(A) General form of the kinetic model used to fit the biosensor responses to EGF stimulation.

(B, C) Best-fit curves (red) and observed responses (open circles) of individual cells expressing EKAR (B) and nucEKAR (C) from E1 of Figure 4A.

(D, E) Statistics of the parameters and graphs showing all individual traces (thin black), average data (bold black)  $\pm$  SD (blue), and data fit (red) for EKAR (D) and nucEKAR (E). See STAR Methods.

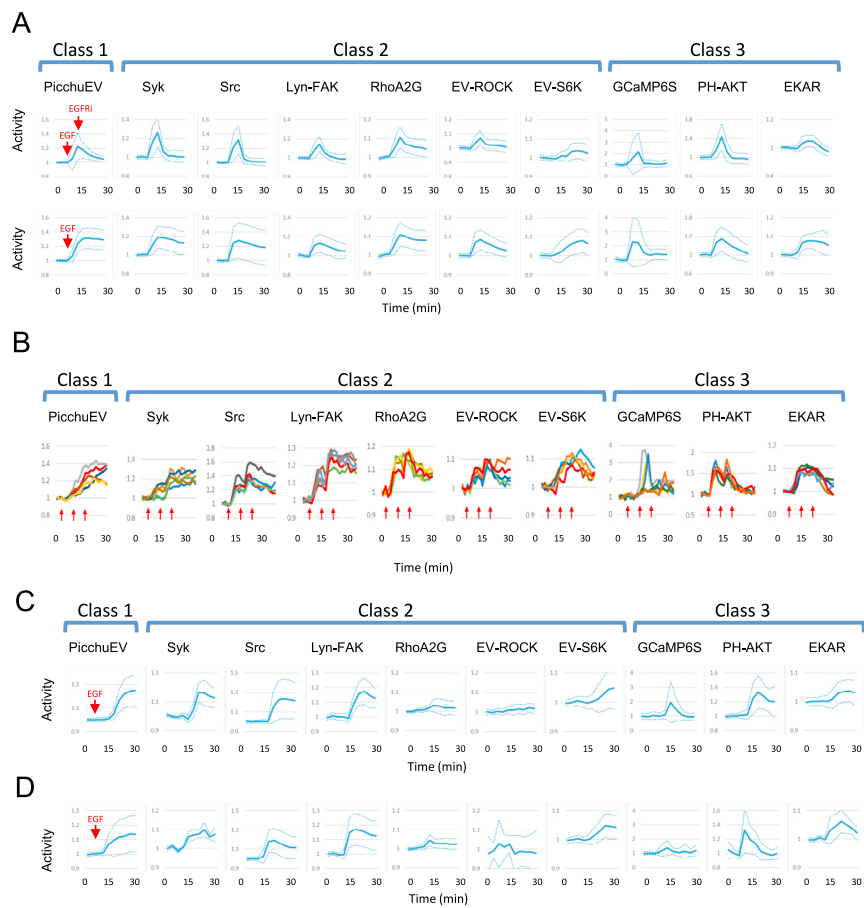


**Figure S5. Response to different patterns of stimulation and cytoskeletal inhibitors, related to Figure 6**

(A) Responses to transient and continued EGF stimulation. (Top) Responses of biosensors obtained from mixed barcoded cells treated with 100 ng/ml EGF at 6 min and 1  $\mu$ M gefitinib (EGFRi) at 12 min. (Bottom) Responses to EGF without EGFRi (adapted from Figure 6C) are shown for comparison. The activities are normalized to the pre-stimulation level. Values represent mean (solid lines)  $\pm$  SD (dashed lines).

(B) Responses to low and high EGF doses in individual cells. Barcoded HeLa cells expressing different biosensors were stimulated with 1, 10 and 100 ng/ml EGF at 6, 21, and 34 min, respectively. Traces of normalized activity from five representative cells expressing indicated biosensors are shown for each biosensor. Red arrows indicate the timing of the three stimuli.

(C) Mixed barcoded cells were pretreated with 5  $\mu$ M jasplakinolide for 30 min, and then stimulated with 10 ng/ml EGF at the indicated time point.

(D) Mixed barcoded cells were pretreated with 5  $\mu$ M latrunculin B for 30 min, and then stimulated with 100 ng/ml EGF at the indicated time point. In (C) and (D), the signals are normalized to the pre-stimulation level, and values represent mean (solid lines)  $\pm$  SD (dashed lines).

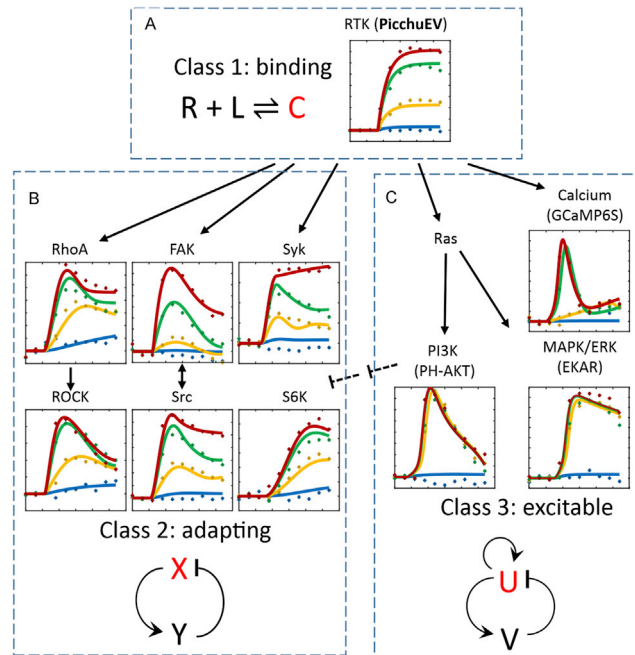


**Figure S6. Network topology of different classes of activities in RTK signaling network, related to Figure 6**

(A-C) Computer simulation (solid lines) of the responses to different doses of stimuli based on a simple binding model for class 1 (A), negative feedback loop for class 2 (B), and excitable network for class 3 (C) biosensors. Schematics of the models are shown, with the variable plotted in the graphs in red. The models were fitted to the mean responses of HeLa cells to different concentrations of EGF (data points represented by dots). See [STAR Methods](#) for details of model fitting.



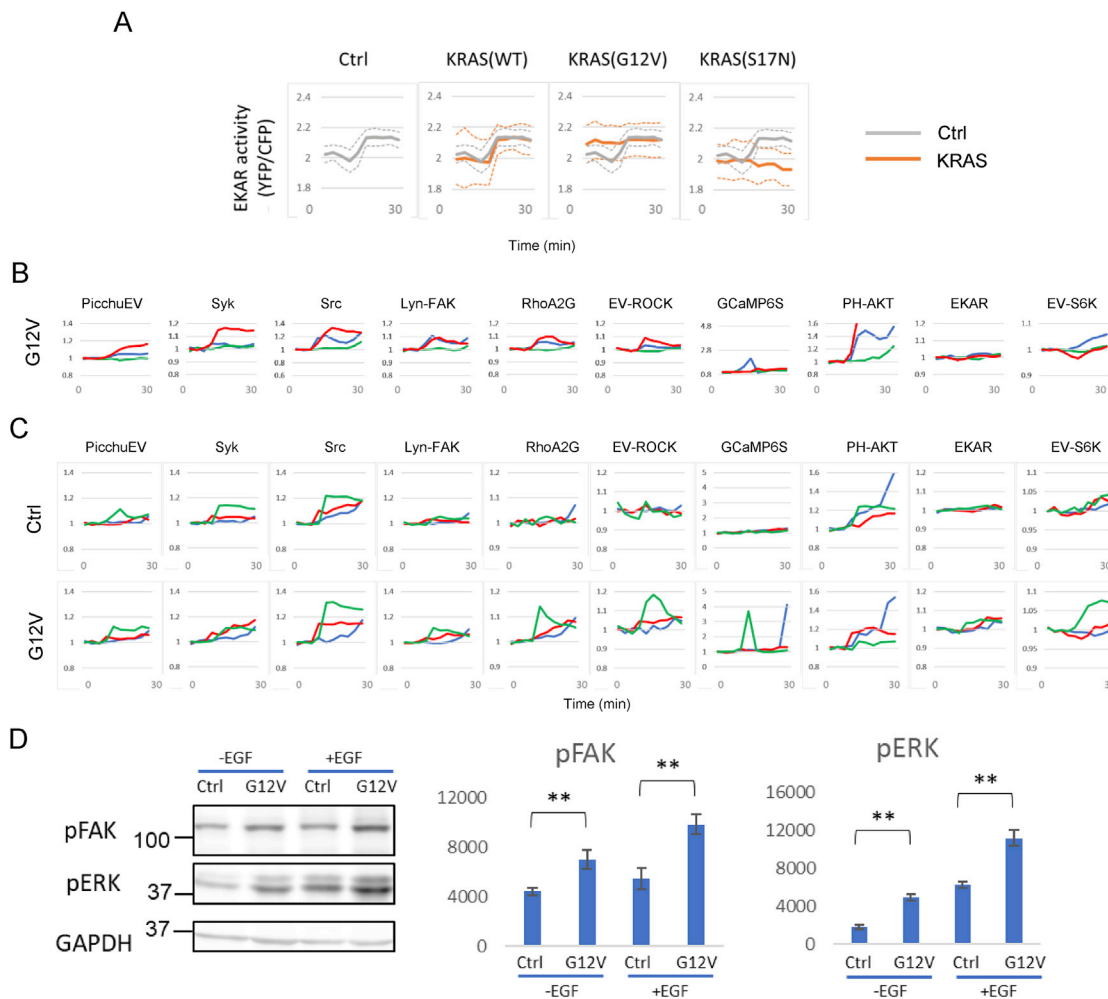


**Figure S7. Effects of KRAS mutants, related to Figure 7**

(A) EKAR activities (mean  $\pm$  SD of YFP/CFP ratio) of mixture of four cell populations: 1) HeLa (Ctrl); 2) HeLa:KRAS(WT), 3) HeLa:KRAS(G12V), and 4) HeLa:KRAS(S17N) stimulated with 100 ng/ml EGF at 6 min.

(B,C) Responses of HeLa:KRAS(G12V) cells (B), and mixture of HeLa (Ctrl) and HeLa:KRAS(G12V) cells (C) to 100 ng/ml EGF added at 6 min. In each set of experiments, traces of the same color are derived from the same experiment (e.g., all the green traces from Ctrl and G12V in (C) are derived from the same cell mixture). The values represent the mean normalized to pre-stimulation levels.

(D) Immunoblots of phospho-FAK, phospho-ERK, and GAPDH using samples from control and KRAS(G12V) cells before and 15 min after stimulation with 100 ng/ml EGF. Error bars: SD. \*\* $p < 0.05$  by Student's *t* test ( $n = 3$ ).